

# Power Analysis for Prediction-Powered Inference

Yiqun T. Chen<sup>1,2</sup>, Moran Guo<sup>1</sup>, and Shengyi Li<sup>1</sup>

<sup>1</sup>Department of Biostatistics, Johns Hopkins University, Baltimore, Maryland 21205, U.S.A.

<sup>2</sup>Department of Computer Science, Johns Hopkins University, Baltimore, Maryland 21205, U.S.A.

yiqun.t.chen@gmail.com

## Abstract

Modern studies increasingly leverage outcomes predicted by machine learning and artificial intelligence (AI/ML) models, and recent work, such as prediction-powered inference (PPI), has developed valid downstream statistical inference procedures. However, classical power and sample size formulas do not readily account for these predictions. In this work, we tackle a simple yet practical question: given a new AI/ML model with high predictive power, how many labeled samples are needed to achieve a desired level of statistical power? We derive closed-form power formulas by characterizing the asymptotic variance of the PPI estimator and applying Wald test inversion to obtain the required labeled sample size. Our results cover widely used settings including two-sample comparisons and risk measures in  $2 \times 2$  tables. We find that a useful rule of thumb is that the reduction in required labeled samples relative to classical designs scales roughly with the  $R^2$  between the predictions and the ground truth. Our analytical formulas are validated using Monte Carlo simulations, and we illustrate the framework in three contemporary biomedical applications spanning single-cell transcriptomics, clinical blood pressure measurement, and dermoscopy imaging. We provide our software as an R package and online calculators at <https://github.com/yiqunchen/pppower>.

**Keywords:** Artificial intelligence; Experimental design; Label efficiency; Power analysis; Prediction-powered inference; Sample size.

## 1 Introduction

Gold-standard labels are fundamental for scientific discoveries but remain time-consuming and expensive: Annotating cell types in single-cell RNA-seq requires expert curation of marker

genes [Baron et al., 2016]; measuring clinical outcomes in randomized trials demands patient follow-up and laboratory assays [Rodger et al., 2012]; and evaluating the quality of large language model (LLM) responses to complex questions needs human expert judgments [Chiang et al., 2024]. At the same time, predictions from machine learning (ML) and artificial intelligence (AI) models have become more accurate and available, where millions of cells can be labeled in minutes, prognostic models can score electronic health records at negligible cost, and “LLM-as-a-judge” pipelines, where an LLM serves as the human expert, can evaluate millions of responses in minutes. With the rise of these models, it is natural to ask whether these predictions can reduce the number of costly labels needed to answer scientific questions of interest, e.g., what is the prevalence of this disease or the change in cell-type proportions across different experimental conditions.

Recent work has shown that treating predicted labels as direct observations is invalid and inflates Type I error. Methods such as *Prediction-Powered Inference* (PPI) [Angelopoulos et al., 2023a] and its tuned variant PPI++ [Angelopoulos et al., 2023b] instead calibrate predictions against a small set of gold-standard labels. Together with related work [Zrnic and Candès, 2024, Miao et al., 2025, Egami et al., 2023, Gronsbell et al., 2024], these methods yield unbiased and asymptotically more efficient estimators than classical analyses based on gold-standard labels alone. However, less work has translated those efficiency gains into the design-stage question every study planner must answer:

*Given a predictive model’s accuracy, how many labeled samples are needed to detect an effect of interest with the desired statistical power?*

Classical power formulas [Erdfelder et al., 1996, Faul et al., 2007] do not provide a straightforward way to distinguish between gold-standard labels and predictions. As a result, practitioners either ignore predictions entirely, which leads to valid planning but potential losses in efficiency, or naively treat predictions as gold-standard labels, which leads to overestimated power and underestimated sample sizes. Several recent contributions start to address this gap: Angelopoulos et al. [2023b] develop cost-allocation routines from pilot data but do not provide closed-form power or sample-size formulas. Comprehensive software packages [Salerno et al., 2025, Egami et al., 2024] unify a range of post-prediction inference methods yet focus on the analysis stage and offer no prospective study-design functionality. Poulet et al. [2025] derive power reductions for ANCOVA-style regression adjustment but restrict attention to that single estimator. While most work focused on comparing asymptotic efficiency of estimators, Mani et al. [2025] also investigated the finite-sample trade-off, and our rule of thumb gives that limitation a concrete planning interpretation. Closest to our work is Broska et al. [2025], who invert the PPI++ variance formula to jointly optimize the

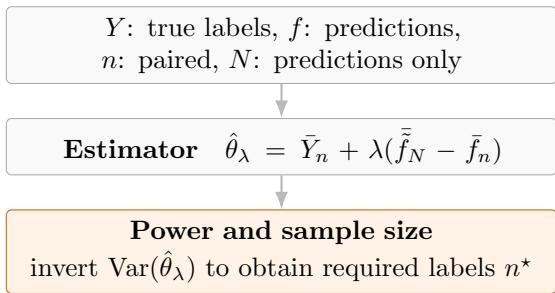
labeled and unlabeled sample sizes under a cost constraint. Our starting point differs in a practical but important way: in many biomedical settings the two sample sizes are *not* jointly optimized. The pool of unlabeled observations is often fixed by the experiment itself (e.g., the number of cells captured in a single-cell assay, or the patients meeting inclusion criteria), and the binding constraint is how many a biologist or physician can manually label. We therefore condition on a given  $N$  and ask how many gold-standard labels  $n$  are needed to achieve target power.

In this paper, we propose `pppower`, a framework and R package for prediction-powered power analysis (see Figure 1). Our contributions are as follows:

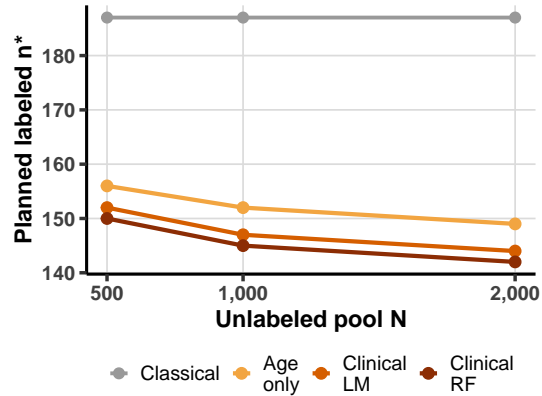
1. **Closed-form formulas.** We derive power and sample-size formulas for prediction-powered estimators that combine a smaller set of gold-standard labels with a larger pool of model-based predicted labels, and show that they reduce to the classical formulas when the predictions are uninformative. These formulas cover two-sample comparisons, paired designs, odds ratios and relative risks in  $2 \times 2$  tables, and regression contrasts for (generalized) linear models (Propositions 1–6, 7, and 8). A simple rule of thumb emerges: the required labeled sample size drops by approximately  $R^2 \times 100\%$ .
2. **User-friendly parameterization.** The formulas accept  $R^2$ , sensitivity/specificity, or confusion matrices as inputs for the one-sample and binary-table designs, avoiding direct covariance specification in the main operational cases; regression-contrast extensions still require contrast-level pilot covariance blocks (Sections 3.3 and 4.4).
3. **Simulation validation.** A comprehensive simulation study validates all formulas against Monte Carlo estimates and establishes practical guidance on when model-based predicted labels yield the largest reductions in required labeled sample size (Section 5).
4. **Open-source software with case study.** An R package with a `pwr`-style API and an accompanying online calculator unify power calculation and sample-size determination in a single function call. We demonstrate the package on three biomedical case studies (Section 6).

## 2 Setup and Background

We consider i.i.d. labeled data  $\{(X_i, Y_i)\}_{i=1}^n$  drawn from a joint distribution  $P_{XY}$  on  $\mathcal{X} \times \mathcal{Y}$ , and an independent pool of unlabeled covariates  $\{\tilde{X}_j\}_{j=1}^N$  drawn from the same marginal  $P_X$ , with  $r = n/N$  denoting the labeled-to-unlabeled ratio. Throughout,  $n$  denotes the



(a) Estimator-and-inversion schematic.



(b) NHANES planning by surrogate model.

Figure 1: Prediction-powered planning. Panel (a) shows the notation, estimator, and variance inversion. Panel (b) shows the NHANES sample-size plan for  $\Delta = 4$  mmHg: gray is the classical design, and the orange curves are the age-only linear model, the richer clinical linear model, and the random forest surrogate.

number of gold-standard labels and  $N$  the size of the larger unlabeled sample carrying model-based predictions, with the practically important regime often having  $N \gg n$ . A predictor  $f : \mathcal{X} \rightarrow \mathcal{Y}$  yields predictions  $f_i = f(X_i)$  on labeled observations and  $\tilde{f}_j = f(\tilde{X}_j)$  on unlabeled ones; we treat  $f$  as independent of both samples (e.g., a pre-trained model), and note that cross-fitting can relax this assumption in practice (see the Supplementary Material and Zrnic and Candès [2024]).

Beyond  $\sigma_Y^2 = \text{Var}(Y)$ , three second-order quantities govern the interplay between outcomes and predictions throughout the paper. The prediction variance  $\sigma_f^2 = \text{Var}(f(X))$  and the residual variance  $\sigma_\varepsilon^2 = \text{Var}(Y - f(X)) = \sigma_Y^2 + \sigma_f^2 - 2\text{Cov}(Y, f)$  together measure how much variation in  $Y$  the predictor captures; the outcome–prediction correlation  $\rho_{Yf} = \text{Cov}(Y, f)/(\sigma_Y\sigma_f)$  summarizes this in a single unitless quantity, with  $\rho_{Yf}^2$  equal to the fraction of  $\sigma_Y^2$  explained by  $f$ . Finally, we define the variance threshold

$$S^2 = \left\{ \Delta / (z_{1-\alpha/2} + z_{1-\beta}) \right\}^2. \quad (1)$$

## 2.1 Testing for One-Sample Mean

We first consider testing equality of the population mean  $\theta^* = \mathbb{E}[Y]$ :

$$H_0 : \theta^* = \theta_0 \quad \text{versus} \quad H_1 : \theta^* = \theta_0 + \Delta, \quad (2)$$

at significance level  $\alpha$  with target power  $1 - \beta$ . The sample mean  $\bar{Y} = n^{-1} \sum_{i=1}^n Y_i$  is unbiased for  $\theta^*$  with variance  $\sigma_Y^2/n$ . The power of the two-sided Wald test for (2) is

$$\text{Power}_{\text{cl}}(n) = \Phi\left(-z_{1-\alpha/2} + \frac{|\Delta|}{\sigma_Y/\sqrt{n}}\right) + \Phi\left(-z_{1-\alpha/2} - \frac{|\Delta|}{\sigma_Y/\sqrt{n}}\right). \quad (3)$$

Inverting (3) by dropping the negligible second term gives  $n_{\text{cl}} \geq \sigma_Y^2/S^2$ . For fixed  $\alpha$ ,  $\beta$ , and  $\Delta$ ,  $\sigma_Y^2$  is the only determinant of the required sample size: reducing it is the only way to increase power for a fixed  $n$ .

## 2.2 Recap of Prediction-Powered Inference

The classical power formula in (3) cannot directly make use of the predictions  $\tilde{f}$ . In this section, we first review the PPI and PPI++ estimators and their variances, which can then be inverted to obtain the power formulas using both gold-standard labels and predictions.

When the population mean is the target of interest, the PPI estimator [Angelopoulos et al., 2023a] makes a simple observation that the population mean decomposes as  $\theta^* = \mathbb{E}[f(X)] + \mathbb{E}[Y - f(X)]$ , and each component can be estimated separately:

$$\hat{\theta}_{\text{PPI}} = \underbrace{\frac{1}{N} \sum_{j=1}^N \tilde{f}_j}_{\text{unlabeled mean}} + \underbrace{\frac{1}{n} \sum_{i=1}^n (Y_i - f_i)}_{\text{labeled correction}}. \quad (4)$$

**Proposition 1 (Mean PPI++ variance)** *Under our setup, the PPI estimator is unbiased and asymptotically normal with variance*

$$\text{Var}(\hat{\theta}_{\text{PPI}}) = \frac{\sigma_f^2}{N} + \frac{\sigma_\varepsilon^2}{n}. \quad (5)$$

The two terms reflect prediction noise  $\sigma_f^2/N$  from the unlabeled sample and residual noise  $\sigma_\varepsilon^2/n$  from the labeled sample. When  $N$  is large, the variance is dominated by  $\sigma_\varepsilon^2/n$ .

While PPI in (4) uses  $f_i$ , the resulting estimator remains unbiased if we replace  $f_i$  with any function  $g(f_i)$ , and an appropriate choice of  $g$  could further reduce the variance. PPI++ [Angelopoulos et al., 2023b] considers  $g(f_i) = \lambda f_i$  with a tunable parameter  $\lambda \in \mathbb{R}$  controlling the weight placed on predictions:

$$\hat{\theta}_\lambda = n^{-1} \sum_{i=1}^n Y_i + \lambda \left( N^{-1} \sum_{j=1}^N \tilde{f}_j - n^{-1} \sum_{i=1}^n f_i \right). \quad (6)$$

The asymptotic variance of  $\widehat{\theta}_\lambda$  is

$$\text{Var}(\widehat{\theta}_\lambda) = \frac{\sigma_Y^2}{n} + \lambda^2 \sigma_f^2 \left( \frac{1}{N} + \frac{1}{n} \right) - \frac{2\lambda \text{Cov}(Y, f)}{n}, \quad (7)$$

and the asymptotic-variance-minimizing tuning parameter is

$$\lambda^* = \frac{\text{Cov}(Y, f)}{(1+r)\sigma_f^2}, \quad (8)$$

with resulting optimal variance

$$\text{Var}(\widehat{\theta}_{\lambda^*}) = \frac{\sigma_Y^2}{n} - \frac{\text{Cov}(Y, f)^2}{\sigma_f^2} \cdot \frac{N}{n(n+N)}. \quad (9)$$

### 3 Power and Sample Size for PPI++

Since PPI is the special case of PPI++ with  $\lambda = 1$ , we state all results for general  $\lambda$ ; setting  $\lambda = 1$  recovers the PPI-specific results. The optimal variance (9) plays the same role for PPI++ that  $\sigma_Y^2/n$  plays for the classical estimator: it determines the power of the Wald test.

#### 3.1 Tests for a One-Sample Mean

**Proposition 2 (PPI++ power)** Consider testing (2) using the Wald statistic  $Z = (\widehat{\theta}_{\lambda^*} - \theta_0) / \sqrt{\text{Var}(\widehat{\theta}_{\lambda^*})}$ . Recalling  $\text{Var}(\widehat{\theta}_{\lambda^*})$  from (9), the power of the two-sided test at level  $\alpha$  is

$$\text{Power}_{\text{PPI}}(n, N) = \Phi \left( -z_{1-\alpha/2} + \frac{|\Delta|}{\sqrt{\text{Var}(\widehat{\theta}_{\lambda^*})}} \right) + \Phi \left( -z_{1-\alpha/2} - \frac{|\Delta|}{\sqrt{\text{Var}(\widehat{\theta}_{\lambda^*})}} \right). \quad (10)$$

Inverting (10) by setting  $\text{Var}(\widehat{\theta}_{\lambda^*}) \leq S^2$  and solving the resulting quadratic in  $n$  yields the following sample-size formula.

**Proposition 3 (PPI++ sample size)** The minimum labeled sample size required to achieve power  $1 - \beta$  is

$$n \geq \frac{\sigma_Y^2 - S^2 N + \sqrt{(\sigma_Y^2 - S^2 N)^2 + 4S^2 N \sigma_Y^2 (1 - \rho_{Yf}^2)}}{2S^2}. \quad (11)$$

We write  $n^*$  for the smallest integer labeled sample size satisfying (11), that is, the inverted minimum number of gold-standard labels needed to attain the target power. For

fixed  $N$ , the inversion in (11) can return  $n^* > N$ . This does not invalidate the variance formula; it simply means that a fixed-pool design would exhaust the available prediction pool. Such a regime may be of limited practical interest, as the motivating assumption is that the main constraint lies in the cost of obtaining gold-standard labels.

**Corollary 4 (Rule of thumb)** *In the regime  $N \gg n$ , the term  $\sigma_f^2/N$  becomes negligible and the optimal variance reduces to  $\text{Var}(\hat{\theta}_{\lambda^*}) \approx \sigma_Y^2(1 - \rho_{Yf}^2)/n$ , yielding the simple approximation  $n_{\text{PPI}}/n_{\text{cl}} \approx 1 - \rho_{Yf}^2$ .*

**Rule of thumb.** A predictor with  $R^2 = \rho_{Yf}^2$  reduces the required labeled sample size by approximately  $R^2 \times 100\%$ . For example,  $R^2 = 0.5$  halves the labeled-data requirement, and  $R^2 = 0.9$  yields up to a 90% reduction.

### 3.2 Connection to Semiparametric Efficiency

The family of estimators  $n^{-1} \sum_{i=1}^n Y_i - n^{-1} \sum_{i=1}^n g(f_i) + N^{-1} \sum_{j=1}^N g(\tilde{f}_j)$  is unbiased for  $\theta^*$  for any function  $g$ , and the choice of  $g$  governs the asymptotic variance. For the mean functional, choosing  $g(f) = \mathbb{E}[Y | f]$  minimizes the asymptotic variance not merely within this family but among all asymptotically unbiased estimators of  $\theta^*$ , a direct consequence of classical semiparametric efficiency theory. In this one-sample mean setting, the factor  $1 - \rho_{Yf}^2$  in the rule of thumb above represents the fundamental limit on how much predictions can help: it is the efficiency bound, not just the performance of a particular estimator.

In the special case where  $Y$  and  $f(X)$  are both binary, the linear construction with optimal  $\lambda$  achieves this bound, so PPI++ is semiparametrically efficient. In more general settings the linear form may be suboptimal [Chen et al., 2026, Ji et al., 2025, Xu et al., 2025, Song et al., 2026], and the variance-optimal estimator could replace  $\lambda f_i$  with a non-linear estimate  $\hat{g}(f_i)$  of  $\mathbb{E}[Y | f]$ , which can be estimated from the labeled data. In this case, the same set of arguments holds but the estimated variance will differ.

### 3.3 Calibration from Common Metrics

For the one-sample mean formulas above, the prediction enters through  $\text{Cov}(Y, f)^2/\sigma_f^2 = \sigma_Y^2 \rho_{Yf}^2$ , so the key planning inputs reduce to the outcome variance  $\sigma_Y^2$  and the squared outcome–prediction correlation  $\rho_{Yf}^2$ . In practice, however, ML model documentation does not always report these quantities directly: continuous models are typically summarized by held-out  $R^2$ , while classifiers are characterized by metrics such as accuracy, precision, and recall.

**Continuous outcomes.** When the model  $R^2$  is reported in prior publications, we can use  $R^2 = \rho_{Yf}^2$  directly. Many software packages instead report the mean-squared error  $\sigma_\varepsilon^2 = \sigma_Y^2 + \sigma_f^2 - 2\text{Cov}(Y, f)$ . This summary does not identify  $\sigma_f^2$  and  $\text{Cov}(Y, f)$  separately, but it still gives a conservative planning input: by Cauchy–Schwarz,  $\sigma_\varepsilon^2 \geq \sigma_Y^2(1 - \rho_{Yf}^2)$ , so  $R^2 \leq \rho_{Yf}^2$ . Thus plugging such an  $R^2$  into the rule of thumb, or into (11) through  $\rho_{Yf}^2 \approx R^2$ , will give us a more conservative estimate of the number of required samples.

**Binary outcomes.** For a binary outcome  $Y \in \{0, 1\}$  and a binary classifier  $f \in \{0, 1\}$ , the required variance components are determined by three quantities: the outcome prevalence  $p = P(Y = 1)$ , the sensitivity  $\text{se} = P(f = 1 | Y = 1)$  and the specificity  $\text{sp} = P(f = 0 | Y = 0)$ . From these, the prediction prevalence is  $p_f = \text{se} \cdot p + (1 - \text{sp})(1 - p)$ , and the three inputs follow as  $\sigma_Y^2 = p(1 - p)$ ,  $\sigma_f^2 = p_f(1 - p_f)$ , and  $\text{Cov}(Y, f) = \text{se} \cdot p - p \cdot p_f$ .

## 4 Extensions to Other Designs

We next extend the one-sample framework of Section 3 to other commonly used designs: two-sample comparisons (unpaired and paired),  $2 \times 2$  table tests, and contrasts for linear and logistic models.

### 4.1 Tests for Equality of Two Means

Consider comparing two independent groups  $A$  and  $B$  with population means  $\theta_A^*$  and  $\theta_B^*$ , where the parameter of interest is  $\theta_A^* - \theta_B^*$ . For each group  $g \in \{A, B\}$ , we observe  $n_g$  labeled pairs and  $N_g$  unlabeled observations, and construct a group-specific PPI++ estimator  $\hat{\theta}_{g,\text{PPI}}$  as in (6). The PPI++ estimator of the group difference is

$$\hat{\Delta}_{\text{PPI}} = \hat{\theta}_{A,\text{PPI}} - \hat{\theta}_{B,\text{PPI}}. \quad (12)$$

**Proposition 5 (Two-sample PPI++ variance)** *Under independent groups, the variance of  $\hat{\Delta}_{\text{PPI}}$  at the group-specific oracle tuning parameters is*

$$\text{Var}(\hat{\Delta}_{\text{PPI}}) = \sum_{g \in \{A, B\}} \left[ \frac{\sigma_{Y,g}^2}{n_g} - \frac{\text{Cov}(Y_g, f_g)^2}{\sigma_{f,g}^2} \cdot \frac{N_g}{n_g(n_g + N_g)} \right]. \quad (13)$$

*In the regime  $N_A, N_B \gg n_A, n_B$ , this reduces to*

$$\text{Var}(\hat{\Delta}_{\text{PPI}}) \approx \frac{\sigma_{Y,A}^2(1 - \text{Corr}(Y_A, f_A)^2)}{n_A} + \frac{\sigma_{Y,B}^2(1 - \text{Corr}(Y_B, f_B)^2)}{n_B}, \quad (14)$$

which is the sum of the group-specific one-sample variances, each reduced by the squared outcome–prediction correlation within that group.

The required sample sizes  $n_A$  and  $n_B$  follow from setting  $\text{Var}(\widehat{\Delta}_{\text{PPI}}) \leq S^2$  from (1) and specifying an allocation ratio  $n_A/n_B$ ; for a balanced design ( $n_A = n_B = n$ ) the condition becomes  $n \geq [\sigma_{Y,A}^2(1 - \text{Corr}(Y_A, f_A)^2) + \sigma_{Y,B}^2(1 - \text{Corr}(Y_B, f_B)^2)]/S^2$ .

## 4.2 Tests for Paired Mean Differences

In paired designs, each subject  $i$  contributes measurements under both conditions (e.g., before and after treatment), yielding within-subject differences  $Y_i^A - Y_i^B$  with paired predictions  $f^A(X_i) - f^B(X_i)$ . The parameter of interest is  $\mathbb{E}[Y^A - Y^B]$ , and the problem reduces directly to the one-sample framework applied to the differences.

**Proposition 6 (Paired PPI++ variance)** *Let  $D_i = Y_i^A - Y_i^B$  and  $G_i = f_i^A - f_i^B$ . Applying the one-sample PPI++ result to the paired differences gives*

$$\text{Var}(\widehat{\Delta}_{\text{PPI}++}) = \frac{\text{Var}(D)}{n} - \frac{\text{Cov}(D, G)^2}{\text{Var}(G)} \cdot \frac{N}{n(n+N)} = \frac{\text{Var}(D)}{n} \left( 1 - \text{Corr}(D, G)^2 \frac{N}{n+N} \right).$$

When  $N \gg n$ , this becomes  $\text{Var}(\widehat{\Delta}_{\text{PPI}++}) \approx \text{Var}(Y^A - Y^B) \{1 - \text{Corr}(Y^A - Y^B, f^A - f^B)^2\} / n$ .

Just as a paired design can be more efficient than an unpaired two-sample test by removing between-subject noise, the correlation  $\text{Corr}(Y^A - Y^B, f^A - f^B)$  governs the efficiency gain here and can differ substantially from the marginal correlations  $\text{Corr}(Y_A, f_A)$  and  $\text{Corr}(Y_B, f_B)$ : if the predictor captures within-subject variation well, this correlation can be high even when the marginal correlations are moderate, and conversely.

## 4.3 Tests for Relative Risk and Odds Ratio in $2 \times 2$ Tables

Many clinical and epidemiological studies compare whether a binary event occurs in two groups, such as treatment ( $g = 1$ ) and control ( $g = 0$ ). For each group  $g$ , the labeled data contain event indicators  $Y_{gi} \in \{0, 1\}$ , while the prediction model produces a surrogate  $f_g(X)$  for that same event indicator on both the labeled and unlabeled subjects in that group. This setup is often summarized as a  $2 \times 2$  table of aggregated counts indexed by the group label  $g$  and the outcome  $Y$ .

The two standard effect measures in this setting are  $\text{RR} = \frac{p_1}{p_0}$ ,  $\text{OR} = \frac{p_1/(1-p_1)}{p_0/(1-p_0)}$ , and under the null hypothesis that the treatment  $g$  has no effect, we would have  $\text{RR} = \text{OR} = 1$ . In

practice, we often consider the equivalent formulation on the log scale using  $\log(\text{RR}) = \log p_1 - \log p_0$  and  $\log(\text{OR}) = \text{logit}(p_1) - \text{logit}(p_0)$ .

As both estimands only depend on the group-specific event probability  $p_g = P(Y = 1 \mid G = g)$ , it suffices to estimate  $p_g$  using  $\hat{p}_{g,\lambda_g} = \bar{Y}_{L,g} + \lambda_g(\bar{f}_{U,g} - \bar{f}_{L,g})$ . Here,  $\bar{Y}_{L,g}$  is the labeled event rate, and  $\bar{f}_{L,g}$  and  $\bar{f}_{U,g}$  are the average predictions in the labeled and unlabeled samples from group  $g$ . Under our independence assumption, the asymptotic variance of  $\log \widehat{\text{RR}}$  and  $\log \widehat{\text{OR}}$  follows directly from the delta method.

**Proposition 7 (PPI++ sample size for relative risk and odds ratio)** *Assume the two groups are independent, let  $\rho_g = \text{Corr}(Y_g, f_g)$ , and fix an allocation ratio  $\kappa = n_1/n_0$ . In the regime  $N_g \gg n_g$ , define  $\Delta_{\text{RR}} = \log(p_1/p_0)$ ,  $\Delta_{\text{OR}} = \text{logit}(p_1) - \text{logit}(p_0)$ ,  $S_{\text{RR}}^2 = \Delta_{\text{RR}}^2/(z_{1-\alpha/2} + z_{1-\beta})^2$ , and  $S_{\text{OR}}^2 = \Delta_{\text{OR}}^2/(z_{1-\alpha/2} + z_{1-\beta})^2$ . Then*

$$\begin{aligned} \text{Var}(\log \widehat{\text{RR}}) &\approx \frac{1}{n_0} \left[ \frac{(1-p_0)(1-\rho_0^2)}{p_0} + \frac{1}{\kappa} \frac{(1-p_1)(1-\rho_1^2)}{p_1} \right], \\ \text{Var}(\log \widehat{\text{OR}}) &\approx \frac{1}{n_0} \left[ \frac{1-\rho_0^2}{p_0(1-p_0)} + \frac{1}{\kappa} \frac{1-\rho_1^2}{p_1(1-p_1)} \right]. \end{aligned}$$

Consequently, the minimum labeled sample sizes required for a two-sided Wald test at level  $\alpha$  with power  $1 - \beta$  are

$$\begin{aligned} n_0^{\text{RR}} &\geq \frac{1}{S_{\text{RR}}^2} \left[ \frac{(1-p_0)(1-\rho_0^2)}{p_0} + \frac{1}{\kappa} \frac{(1-p_1)(1-\rho_1^2)}{p_1} \right], & n_1^{\text{RR}} &= \kappa n_0^{\text{RR}}, \\ n_0^{\text{OR}} &\geq \frac{1}{S_{\text{OR}}^2} \left[ \frac{1-\rho_0^2}{p_0(1-p_0)} + \frac{1}{\kappa} \frac{1-\rho_1^2}{p_1(1-p_1)} \right], & n_1^{\text{OR}} &= \kappa n_0^{\text{OR}}. \end{aligned}$$

For balanced designs, set  $\kappa = 1$ . Setting  $\rho_0 = \rho_1 = 0$  recovers the classical relative-risk and odds-ratio sample-size formulas.

## 4.4 Tests for Regression Contrasts in Generalized Linear Models

Many of the power analyses above can be recast as testing a linear contrast in a generalized linear model. We first motivate prediction-powered inference for linear models. Consider the ordinary least squares (OLS) estimator with target coefficient vector  $\beta^*$  that minimizes  $\mathbb{E}[(Y - X^\top \beta)^2]$ . The normal equations imply  $\mathbb{E}[X X^\top] \beta^* = \mathbb{E}[X Y]$ .

Now, for covariate–outcome observation pairs  $(x_i, y_i)$ , if  $f(x_i)$  is a prediction of  $y_i$ , we can decompose the normal equation as  $\mathbb{E}[X Y] = \mathbb{E}[X f(X)] + \mathbb{E}[X \{Y - f(X)\}]$ , which leads to

the estimating equation

$$\frac{1}{n} \sum_{i=1}^n X_i(Y_i - X_i^\top \beta) + \lambda \left[ \frac{1}{N} \sum_{j=1}^N \tilde{X}_j(\tilde{f}_j - \tilde{X}_j^\top \beta) - \frac{1}{n} \sum_{i=1}^n X_i(f_i - X_i^\top \beta) \right] = 0.$$

Similarly, for a generalized linear model with mean function  $\mu_\beta(X)$ , the target parameter satisfies the score equation  $\mathbb{E}[X\{Y - \mu_\beta(X)\}] = 0$  at  $\beta = \beta^*$ , motivating the decomposition

$$\mathbb{E}[X\{Y - \mu_\beta(X)\}] = \mathbb{E}[X\{\mu_f(X) - \mu_\beta(X)\}] + \mathbb{E}[X\{Y - \mu_f(X)\}],$$

which yields the analogous PPI++ score equation

$$\frac{1}{n} \sum_{i=1}^n X_i(Y_i - \mu_\beta(X_i)) + \lambda \left[ \frac{1}{N} \sum_{j=1}^N \tilde{X}_j(\mu_f(\tilde{X}_j) - \mu_\beta(\tilde{X}_j)) - \frac{1}{n} \sum_{i=1}^n X_i(\mu_f(X_i) - \mu_\beta(X_i)) \right] = 0.$$

With  $r = n/N$ , a first-order expansion of  $\hat{\theta}_\lambda$  gives

$$\text{Var}(\hat{\theta}_\lambda) \approx \frac{V_{YY} + \lambda^2(1+r)V_{ff} - 2\lambda V_{Yf}}{n},$$

where  $V_{YY}$ ,  $V_{ff}$ , and  $V_{Yf}$  denote the contrast-level variances of the labeled score term, the prediction term, and their covariance.

Below, in Proposition 8, we summarize the power and required sample size for the contrast of interest  $\theta^* = a^\top \beta^*$  using the PPI++ estimator.

**Proposition 8 (PPI++ sample size for regression contrasts)** *Let  $\Delta = a^\top \beta^*$  denote the target contrast under the alternative. The oracle tuning parameter is  $\lambda^* = V_{Yf}/\{(1+r)V_{ff}\}$ , which yields*

$$\text{Var}(\hat{\theta}_{\lambda^*}) \approx \frac{1}{n} \left( V_{YY} - \frac{V_{Yf}^2}{(1+r)V_{ff}} \right).$$

*Treating  $N$  as fixed, the minimum labeled sample size required for a two-sided Wald test at level  $\alpha$  with power  $1 - \beta$  satisfies*

$$n \geq \frac{V_{YY} - S^2 N + \sqrt{(V_{YY} - S^2 N)^2 + 4S^2 N \left( V_{YY} - \frac{V_{Yf}^2}{V_{ff}} \right)}}{2S^2}.$$

*In the regime  $N \gg n$ , this simplifies to  $n \geq \frac{V_{YY} - V_{Yf}^2/V_{ff}}{S^2}$ .*

## 5 Simulation Studies

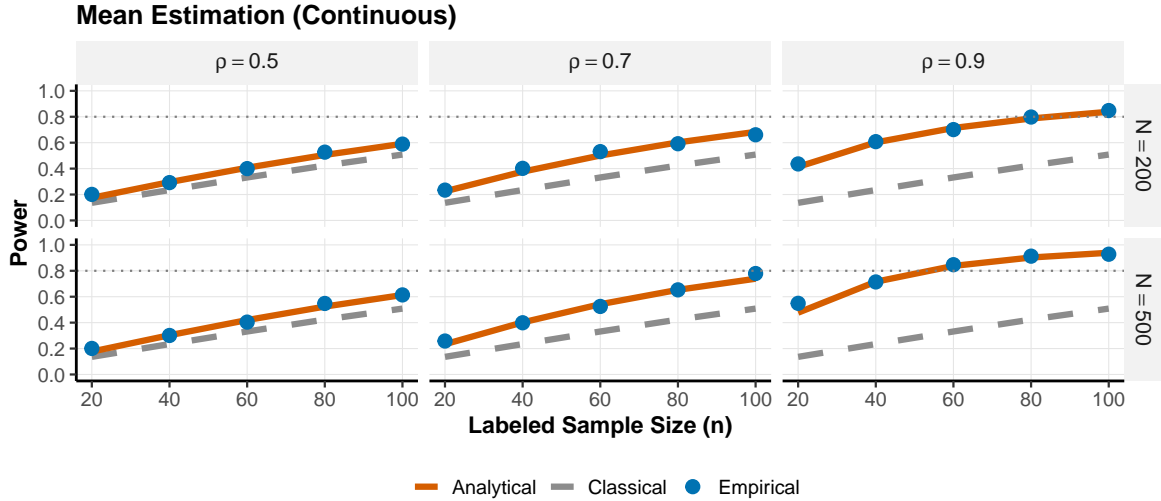
Here, we validate the approximate closed-form formulas derived in Sections 3–4 through comprehensive Monte Carlo simulations. For each scenario, we generate  $R = 1,000$  replicates and compare the empirical power of the PPI++-based tests with the theoretical formulas we presented. Unless otherwise noted, all tests are two-sided at level  $\alpha = 0.05$  and use the oracle  $\lambda^*$ , and we target a power of 80% in the sample size calculations. We also examine several robustness checks, including whether the PPI++-based tests have the correct size (i.e., control Type I error at the nominal level), the discrepancy between the estimated and oracle values of  $\lambda^*$ , and departures from the normality assumptions (e.g., small  $n$  or non-normal outcomes). We present the main power and sample size validation results in the main text, with additional robustness checks deferred to the Supplementary Material.

### 5.1 Power Validation

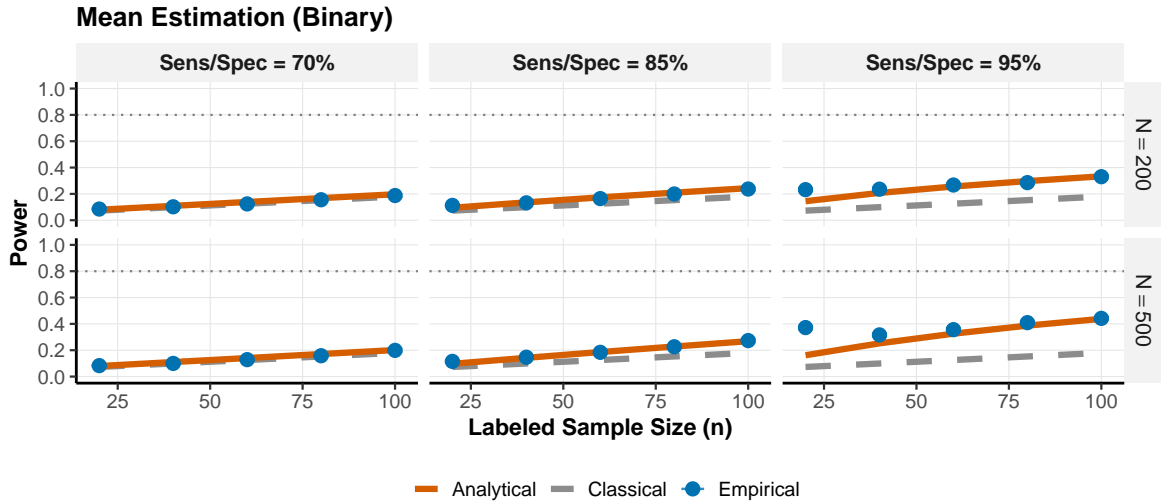
**Mean estimation.** We consider both continuous and binary outcomes. For the continuous case, we simulate  $(Y, f)$  as bivariate normal with  $\sigma_Y^2 = \sigma_f^2 = 1$ , correlation  $\rho \in \{0.5, 0.7, 0.9\}$ , and  $(n, N) \in \{20, 40, 60, 80, 100\} \times \{200, 500\}$ , with a target effect size of  $\Delta = 0.2$ . For the binary outcome experiment, we generate outcomes  $Y \sim \text{Bernoulli}(p = 0.3)$  with predictions generated via sensitivity and specificity conditional on  $Y$ , and  $\Delta = 0.05$ .

Across both settings, power increases as the predictive accuracy of the labels increases (higher  $\rho$ ) and as the number of labeled samples ( $n$ ) increases, and there is strong agreement between the theoretical and empirical power (Figure 2). For binary outcomes, the analytical approximation captures the overall trend, but the smallest- $n$ , highest-accuracy settings show visible finite-sample departures (e.g., sensitivity = specificity = 0.95,  $N = 500$ ,  $n = 20$ ). Our power planning formula is mildly optimistic (about 10% inflation), primarily due to instability in the estimated denominator at very small  $n$ .

**Two-sample tests.** We simulate independent groups with continuous ( $\Delta = 0.3$ ) and binary ( $\Delta = 0.08$ ) outcomes using the same parameter grids as in the mean estimation experiments. Across both outcome types, the theoretical curves track the empirical power closely over the full  $(n, N)$  grid, with maximum absolute discrepancies of 0.02 and 0.03 for continuous and binary outcomes, respectively. The largest deviations typically occur in the most prediction-favorable regimes with very small labeled samples, where the denominator in the estimated variance of the Wald test is again the main source of extra variability. See Figures S1–S2 in the Supplementary Material.



(a) Gaussian outcomes.



(b) Binary outcomes.

Figure 2: One-sample mean validation: empirical power (points, with 95% Monte Carlo error bars for the binary setting) versus theoretical power (lines) for PPI++ with oracle  $\lambda^*$ .

**Paired designs.** Paired continuous and binary designs with within-pair prediction correlation show the same overall pattern of strong agreement between theoretical and empirical power (see Figures S3–S4), with the largest gaps again appearing at small  $n$ . These results suggest that the paired-design approximation remains accurate once the within-pair covariance structure is accounted for.

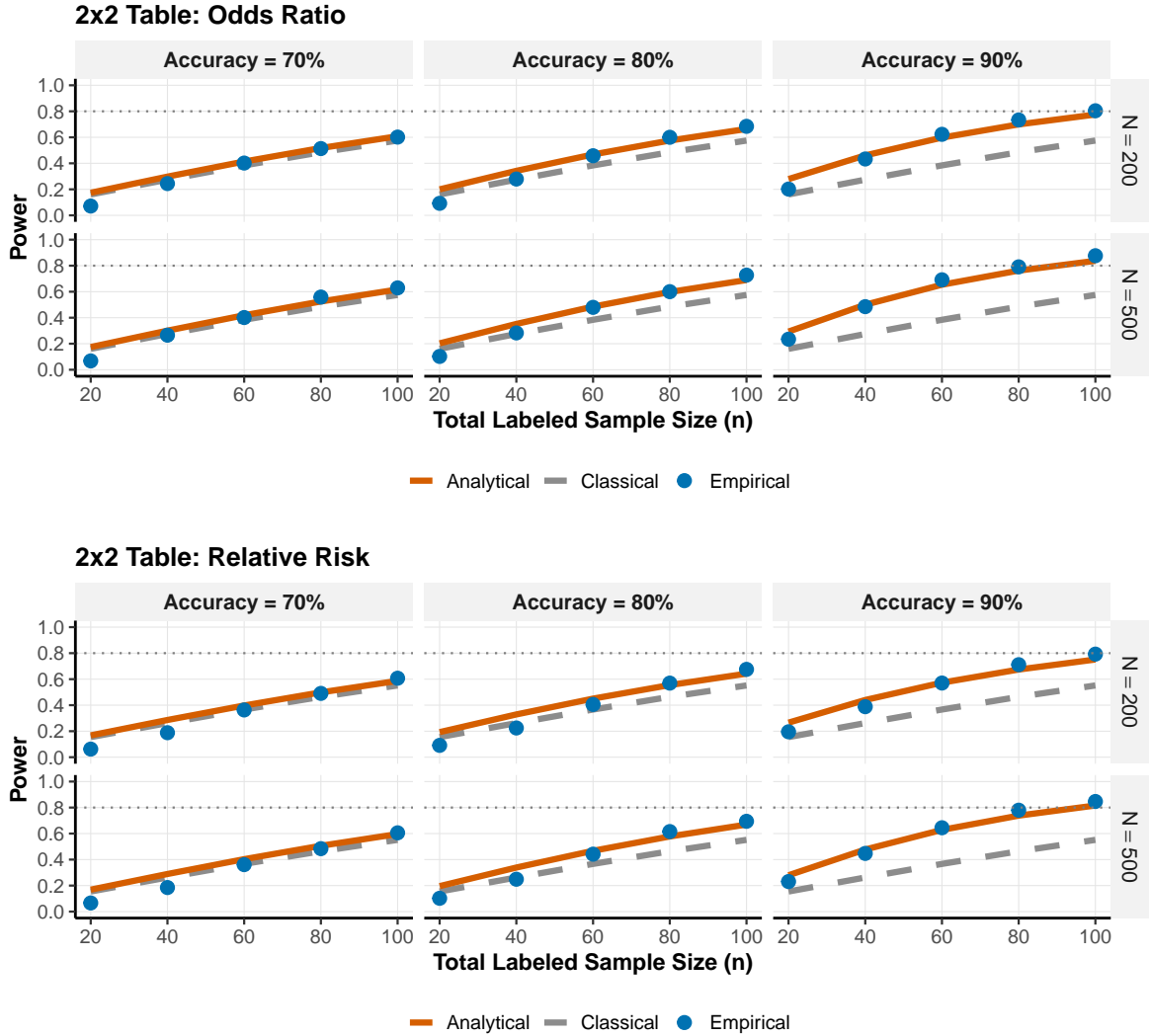


Figure 3: Odds-ratio and relative-risk validation in  $2 \times 2$  tables—analytical (lines) versus empirical (points) PPI++ power for odds ratio (top) and relative risk (bottom). Dashed lines show classical power.

## 5.2 Extensions: $2 \times 2$ Tables and Generalized Linear Models

We next validate the contingency-table and regression extensions developed in Section 4.

**$2 \times 2$  table (odds ratio and relative risk).** The data-generating process draws binary treatment  $X \in \{0, 1\}$  and binary outcome  $Y$  with control probability  $p_{\text{ctrl}} = 0.20$  and experimental probability  $p_{\text{exp}} \in \{0.30, 0.35, 0.40\}$ . A noisy binary classifier with sensitivity = specificity = accuracy serves as the surrogate, with accuracy  $\in \{70\%, 80\%, 90\%\}$ . Figure 3 displays the power result for  $p_{\text{exp}} = 0.40$ , which corresponds to a relative risk of 2.00 and odds ratio of 2.67; agreement is generally tight.

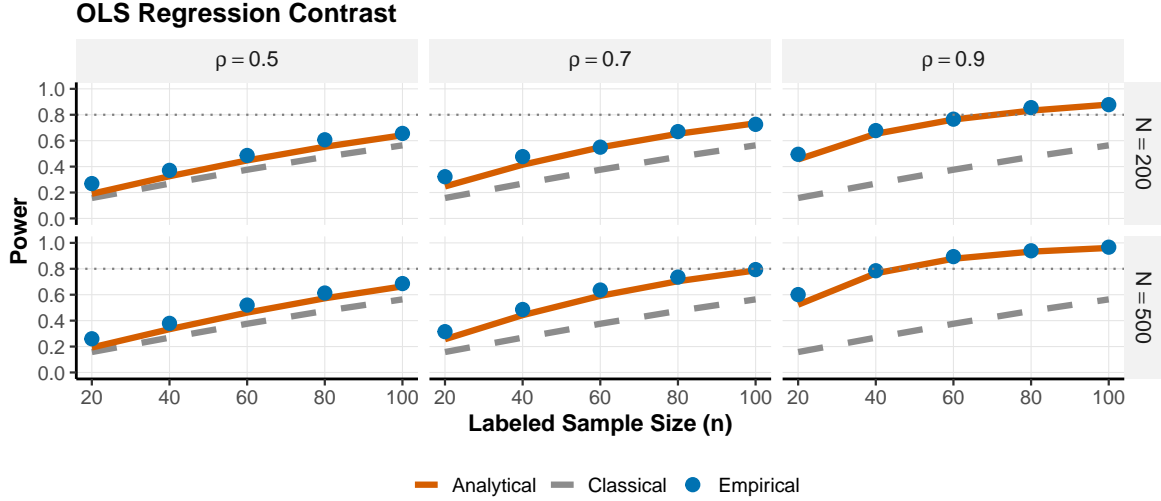
**Linear regression contrast.** We simulate  $X \sim N(0, I_2)$ ,  $Y = X\beta + \varepsilon$  with  $\beta = (\Delta, 0)$ ,  $\Delta = 0.3$ , and predictions  $f = X\beta + \nu$  where  $\nu = \rho\varepsilon + \sqrt{1 - \rho^2}\eta$ ,  $\eta \sim N(0, 1)$ . The contrast  $a = (1, -1)$  tests  $H_0: \beta_1 - \beta_2 = 0$ . Under this simulation setting,  $\text{Var}(a^\top \beta)$  in Proposition 8 reduces to  $V_{YY} = 2$ ,  $V_{ff} = 2$ , and  $V_{Yf} = 2\rho$ . Each Monte Carlo replicate constructs the PPI++ estimator with oracle  $\lambda^*$  and a sandwich estimator for the standard error, then performs a two-sided Wald test. Figure 4(a) shows close agreement across all 30 configurations ( $n \in \{20, 40, 60, 80, 100\}$ ,  $N \in \{200, 500\}$ ,  $\rho \in \{0.5, 0.7, 0.9\}$ ); the maximum discrepancy is 0.08 at small  $n$  where finite-sample sandwich bias is expected.

**Logistic regression contrast.** We extend to non-linear models by simulating  $X \sim N(0, I_2)$ ,  $P(Y=1 | X) = \text{expit}(X\beta)$  with  $\beta = (0.5, 0)$  (corresponding to an odds ratio of  $e^{0.5} \approx 1.65$ ). We consider a noisy binary classifier with sensitivity = specificity = accuracy as the surrogate. Because the required contrast-level variance blocks do not admit convenient closed forms for logistic regression, we approximate the corresponding population quantities once using a large Monte Carlo reference sample ( $M = 100,000$ ) and use them to evaluate the analytical power curve. For the empirical power calculation, each fresh simulated dataset estimates a two-fold cross-fitted plug-in tuning parameter  $\hat{\lambda}$  and then solves the corresponding rectified score equation using that plug-in estimate. Figure 4(b) displays results across 30 configurations ( $n \in \{20, 40, 60, 80, 100\}$ ,  $N \in \{200, 500\}$ , accuracy  $\in \{70\%, 80\%, 90\%\}$ ); the maximum discrepancy is 0.1, concentrated at small  $n$  with high accuracy where estimating  $\hat{\lambda}$  adds the most finite-sample variability.

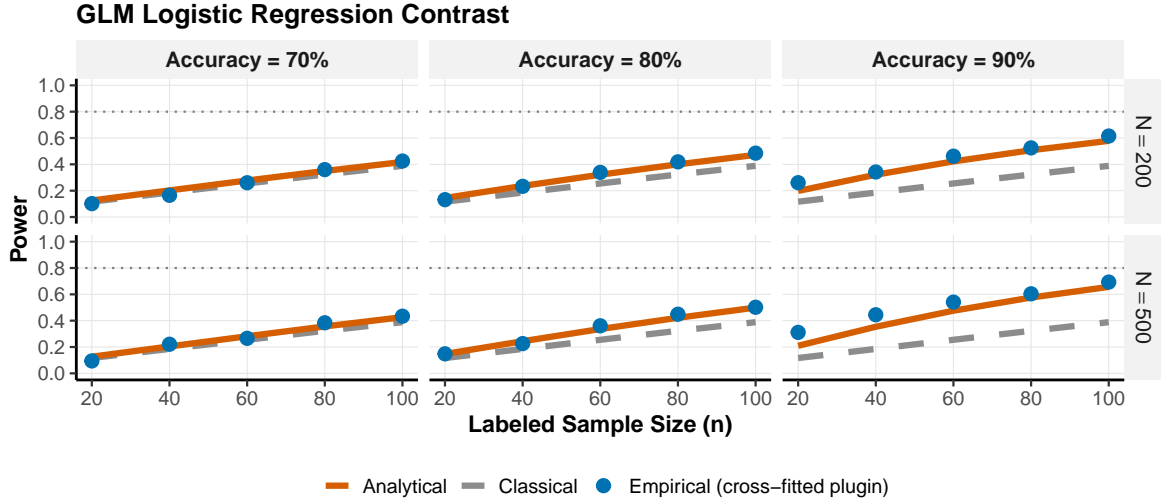
### 5.3 Robustness Checks

We also examine sample-size inversion accuracy, Type I error control of the PPI++ tests, and departures from Gaussian assumptions. Fixing target power in  $\{0.60, 0.70, 0.80, 0.90\}$  shows that the planned integer sample size  $n^*$  delivers achieved power close to target across the one-sample, two-sample, and paired designs; analytical deviations are uniformly small, and empirical deviations are only modest in the smallest- $n$  cells (Figure S5 in the Supplementary Material). We also verified that, under the null, rejection rates remain close to the nominal 0.05 level, ranging from 0.04 to 0.06 in the continuous and binary settings (Figure S7 in the Supplementary Material). Moreover, with  $N = 1,000$  fixed, the plug-in estimate of the tuning parameter  $\hat{\lambda}$  converges steadily toward the oracle  $\lambda^*$  as  $n$  grows (Figure S8 in the Supplementary Material).

We next stress the formulas through practical implementation choices and finite-sample perturbations around the Gaussian benchmark. Replacing the oracle tuning parameter by the plugin estimate  $\hat{\lambda}$  changes power very little on the Gaussian one-sample settings: the



(a) OLS beta-coefficient contrast validation.



(b) Logistic-regression contrast validation.

Figure 4: Regression-contrast validation: analytical (lines) versus empirical (points) PPI++ power. In panel (b), the empirical logistic-regression points use a two-fold cross-fitted plug-in  $\hat{\lambda}$  estimated within each replicate, while the analytical curve uses the large-reference-sample approximation. Dashed lines show the corresponding classical power curves.

maximum oracle–plugin difference is 0.03, and both remain close to the analytical curve (Figure S9 in the Supplementary Material). A sweep over effect size  $\Delta \in [0, 0.5]$  at fixed  $N = 500$  produces the expected S-shaped power curves, with larger  $\rho$  shifting the PPI++ curves leftward (Figure S10 in the Supplementary Material). Pushing the Gaussian one-sample design down to  $n \in \{15, 20, 25, 30, 50, 100\}$  shows that the approximation remains usable but is predictably weakest below about  $n = 25$  (Figure S11 in the Supplementary Material),

while varying  $N/n$  from 1 to 100 at fixed  $n = 50$  shows that gains from unlabeled data rise quickly and then saturate around  $N/n \approx 10\text{--}20$  (Figure S12 in the Supplementary Material). For two-sample designs with fixed total labeled and unlabeled budgets, balanced allocation remains best and the analytical curves continue to track the empirical results closely across imbalance ratios (Figure S13 in the Supplementary Material).

Finally, we rerun the one-sample mean experiments under two non-Gaussian outcome distributions on the same  $(n, N, \rho)$  grid. For  $t_5$  outcomes, agreement with the Gaussian-based formula remains tight, with a maximum discrepancy of 0.02. For log-normal outcomes, the approximation remains reasonable once  $n$  is moderate, but the most skewed, small- $n$  configurations show visibly larger departures, with a maximum discrepancy of 0.14. This suggests that moderate heavy tails alone are less problematic, whereas small samples combined with strong skewness can pose challenges for accurate power planning.

## 6 Real Data Applications

In this section, we illustrate the power-analysis workflow on three biomedical datasets: cell-type classification in single-cell RNA-seq [Baron et al., 2016], blood pressure estimation in NHANES 2017–2018 [Centers for Disease Control and Prevention (CDC). National Center for Health Statistics (NCHS), 2020], and melanoma detection in ISIC 2020 dermoscopy images [Rotemberg et al., 2021]. For each dataset, we split the observed data into training, pilot, and evaluation subsets. The prediction models  $f$  are fit on the training split to mimic a pretrained model; the pilot split provides the variance and covariance inputs used to plan the labeled sample size  $n^*$ ; and the evaluation split is treated as an empirical population with full-data truth  $\theta_{\text{eval}}$ . Within each application, we specify a target effect size  $\Delta$  and set the null value to  $\theta_0 = \theta_{\text{eval}} - \Delta$ , so the held-out evaluation split serves as the alternative truth. In all three applications we allocate 25% of the observed data to training, 15% to the pilot split, and the remaining 60% to held-out evaluation. This keeps the pilot meaningfully smaller than the analysis population while still leaving enough data to estimate the planning inputs. For ISIC, where multiple images come from the same patient, this split is done at the patient level to avoid leakage across repeated lesions. Throughout this section, all designs target power 0.80 at level  $\alpha = 0.05$ . Achieved power is estimated empirically from 500 held-out resamples: for the classical design we repeatedly draw  $n_{\text{cl}}$  labeled observations from the evaluation split, while for PPI++ we draw  $n^*$  labeled observations together with  $N$  additional unlabeled observations from the remaining held-out units, apply the corresponding test of  $H_0 : \theta = \theta_0$ , and record the rejection rate.

## 6.1 Cell-Type Classification in Single-Cell RNA-Seq

Baron et al. [2016] constructed a pancreas scRNA-seq atlas that profiles pancreatic cell types across donors. We focus on a simple composition question: among alpha and beta cells, how different are their population shares? Restricting attention to those two cell types, the target estimand is  $\theta = p_\beta - p_\alpha$ , the difference in cell-type proportions. The covariates  $X$  are the cell-level gene-expression profiles used to predict cell identity. We split the 4,851 beta-or-alpha cells into 1,212 training cells, 727 pilot cells, and 2,912 evaluation cells. In the evaluation split,  $p_\beta = 0.521$  and  $p_\alpha = 0.479$ , giving  $\theta_{\text{eval}} = 0.041$ .

To create a meaningful gradient of prediction quality, we compare three prediction rules trained on the training split: a deliberately weak donor-only logistic model that uses only donor identity, a one-gene logistic model using *INS* expression from the Baron data itself, and a random forest fit on the top 20 marker genes ranked within the training split by differential mean log-expression between beta and alpha cells rather than imported from an external marker database. The pilot split is used to estimate the corresponding  $\rho_{Y_f}^2$  values and to plan the labeled sample size for  $\Delta = 0.10$  and  $N \in \{500, 1,000, 2,000\}$ .

The contrast between weak and strong predictions is immediate. At  $N = 500$ , the classical design requires  $n_{\text{cl}} = 785$  labeled cells. The donor-only surrogate has  $\rho_{Y_f}^2 = 0.14$  and yields only a mild reduction to  $n^* = 740$  with achieved power 0.83. By contrast, the *INS* surrogate has  $\rho_{Y_f}^2 = 0.97$  and reduces the plan to  $n^* = 325$ , while the 20-marker random forest reaches  $\rho_{Y_f}^2 = 0.98$  and reduces it further to  $n^* = 306$ , with held-out powers 0.83 and 0.84. These patterns are summarized in Figure 5.

## 6.2 Blood Pressure Estimation from NHANES

Our second case study considers systolic blood pressure in the 2017–2018 NHANES data [Centers for Disease Control and Prevention (CDC), National Center for Health Statistics (NCHS), 2020]. We merge the demographic, anthropometric, and blood-pressure examination files and retain 4,990 adults with complete covariates and at least one systolic blood-pressure measurement. Here,  $Y$  is the mean systolic blood pressure and  $X = (\text{age, sex, race, BMI, waist circumference})$ . The complete dataset is split into 1,247 training observations, 748 pilot observations, and 2,995 evaluation observations; the evaluation mean is  $\theta_{\text{eval}} = 125.9$  mmHg.

We compare three predictive models fit on the training split: an age-only linear model, a richer clinical linear model using all available covariates, and a random forest on all available covariates. The resulting gains are more moderate. At  $N = 2,000$ , the classical design requires  $n_{\text{cl}} = 187$  labeled patients. The age-only model has  $\rho_{Y_f}^2 = 0.22$  and reduces the plan

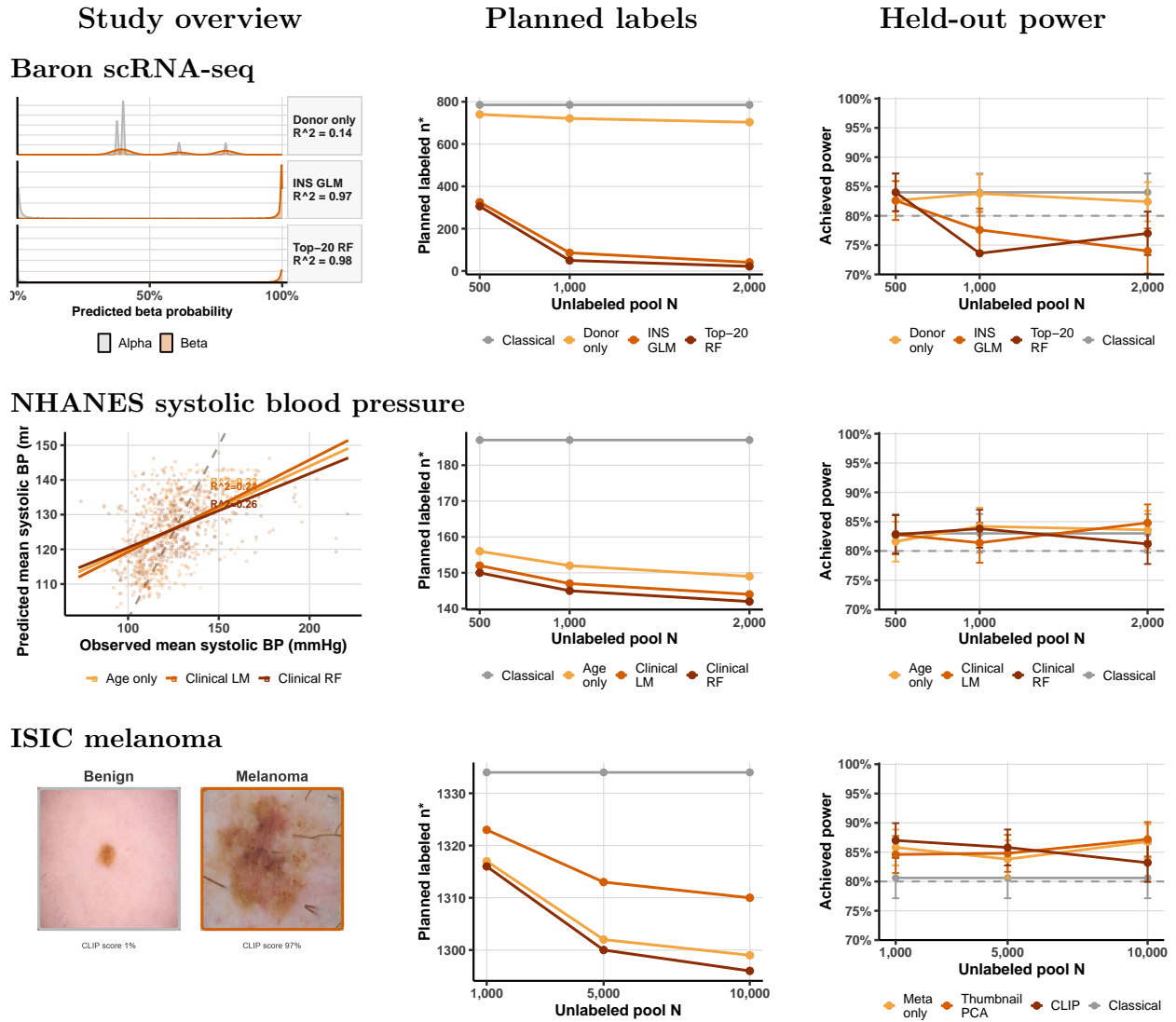


Figure 5: Real-data planning and held-out validation across three biomedical case studies. Each row corresponds to one application (Baron scRNA-seq, NHANES systolic blood pressure, and ISIC melanoma), and the three columns give a study overview, the planned labeled sample size, and the held-out achieved power.

to  $n^* = 149$  with held-out power 0.84. The richer clinical linear model has  $\rho_{Y_f}^2 = 0.24$  and yields  $n^* = 144$  with held-out power 0.85, while the clinical random forest has  $\rho_{Y_f}^2 = 0.26$  and yields  $n^* = 142$  with held-out power 0.81. This case study shows more incremental gains, around 20%, and the smaller pilot split leaves more planning noise in held-out validation.

### 6.3 Melanoma Detection in Dermoscopy Images

Given the global shortage of dermatology resources, screening for skin cancer—especially melanoma—remains time-consuming, expensive, and difficult to scale, contributing to delayed diagnoses and rising treatment burdens. Recent work has shown much promise in automated dermoscopy classifiers for melanoma detection [Daneshjou et al., 2022, Xu et al., 2024, Chen et al., 2024]. For this case study, we use the ISIC 2020 challenge data [Rotemberg et al., 2021], which contains 33,126 dermoscopy images from 2,056 patients with a melanoma prevalence of 1.8%. The target estimand is the mean prevalence. We use the 256-pixel thumbnails of dermoscopy images as well as the accompanying metadata (e.g., age, sex, anatomic site, and patient lesion counts) for a non-image baseline. We split the data at the patient level into 8,609 training images, 5,090 pilot images, and 19,427 evaluation images, corresponding to 514, 308, and 1,234 patients, respectively. The evaluation prevalence is  $\theta_{\text{eval}} = 0.018$ .

We compare three predictors  $f$  trained on the training split: a metadata-only logistic baseline, a logistic model on the top principal components of the image thumbnails, and a logistic regression on the CLIP embeddings [Radford et al., 2021] of the image, which have been shown to perform well in melanoma detection [Xu et al., 2024]. The pilot split is then used to plan the labeled sample size needed to detect an absolute prevalence shift of  $\Delta = 0.01$  with  $N \in \{1,000, 5,000, 10,000\}$  unlabeled images. On the held-out evaluation split, these three models achieve AUROC values of 0.72, 0.79, and 0.83, respectively.

Despite the reasonable AUROCs, this is an intrinsically hard setting with 1.8% population prevalence. The resulting gains are therefore minimal. At  $N = 10,000$ , the classical design requires  $n_{\text{cl}} = 1,334$  pathology-confirmed labels. The metadata-only surrogate yields  $n^* = 1,299$  with held-out power 0.868, the thumbnail-PCA surrogate yields  $n^* = 1,310$  with held-out power 0.872, and the CLIP surrogate yields  $n^* = 1,296$  with held-out power 0.832. Unlike Baron and NHANES, the ISIC case study stays close to the classical regime: even visibly stronger discrimination in the image models does not translate into large planning gains when the outcome is this rare, as the  $\rho_{Y_f}^2$  remains very modest ( $< 0.05$  in all cases).

**Takeaway.** These three examples make the role of the predictive model concrete. In the Baron data, moving from donor-only metadata to expression-based classifiers shifts the design from nearly classical to sharply prediction-powered. In NHANES, all three models lie in

a moderate- $R^2$  regime, so the gains are real but modest. ISIC shows a third regime: even when held-out AUROC improves visibly from metadata to image-based models, the rarity of melanoma leaves the design close to classical. In short, prediction-powered inference is not magic: sample-size reduction is determined by the agreement between predictions and true labels, as measured here by correlation-based summaries.

## 7 Discussion

In this paper, we tackle a practical design question in the era of AI/ML: given a predictive model’s accuracy, how many fewer samples can a study use by leveraging predictions for inference? For the one-sample mean, the rule-of-thumb reduction is around  $R^2$ —a model explaining half of the outcome variation roughly halves the required sample size. Through extensive simulations, we found that our proposed formulas yield theoretical power and sample sizes that closely match the empirical power and sample sizes. Noticeable departures occur at very small sample sizes (fewer than 20 labeled samples) due to high sampling variability. We demonstrate the plug-and-play use of the method on three real-world datasets and open-source our software. Software implementing the formulas is available in the [GitHub repository](#) and in browser-based [sample-size](#) and  $2 \times 2$  planning calculators.

There are several natural extensions of our work. While our current framework largely relies on asymptotic normality, the power analysis literature provides a rich set of small-sample variance and distributional corrections that could improve finite-sample approximations. Similarly, we largely considered the predictor  $f$  to be either pretrained (e.g., ChatGPT or CLIP) or simple enough for cross-fitting to work reliably. A more extensive set of simulations examining finite-sample variance could provide a more precise characterization of these effects. Finally, the prediction-powered inference framework has mostly focused on independent and identically distributed data. Extending the theory, as well as practical sample size design, to more realistic settings with complex designs such as clustered, longitudinal, or survival data is an important next step.

## Acknowledgements

The authors declare no conflict of interest. This work was partially supported by the Johns Hopkins Bloomberg School of Public Health, Department of Biostatistics, Data Science and AI Faculty Innovation Fund and a Google Academic Research Award on AI for Privacy, Safety, and Security.

## Data Availability

Software implementing all methods is available as an R package at <https://github.com/yiqunchen/pppower>. The datasets used in the case studies are publicly available from their original publications: the Baron scRNA-seq data [Baron et al., 2016], the NHANES 2017–2018 data [Centers for Disease Control and Prevention (CDC). National Center for Health Statistics (NCHS), 2020], and the ISIC 2020 dermoscopy data [Rotemberg et al., 2021].

## References

- Anastasios N Angelopoulos, Stephen Bates, Clara Fannjiang, Michael I Jordan, and Tijana Zrnic. Prediction-powered inference. *Science*, 382(6671):669–674, 2023a.
- Anastasios N Angelopoulos, John C Duchi, and Tijana Zrnic. Ppi++: Efficient prediction-powered inference. *arXiv preprint arXiv:2311.01453*, 2023b.
- Maayan Baron, Adrian Veres, Samuel L Wolock, Aubrey L Faust, Renaud Gaujoux, Amedeo Vetere, et al. A single-cell transcriptomic map of the human and mouse pancreas reveals inter-and intra-cell population structure. *Cell Systems*, 3(4):346–360, 2016.
- David Broska, Michael Howes, and Austin van Loon. The mixed subjects design: Treating large language models as potentially informative observations. *Sociological Methods & Research*, 54(3):1074–1109, 2025.
- Centers for Disease Control and Prevention (CDC). National Center for Health Statistics (NCHS). National health and nutrition examination survey data, 2017–2018. <https://www.cdc.gov/nchs/nhanes/continuousnhanes/default.aspx?BeginYear=2017>, 2020. Hyattsville, MD: U.S. Department of Health and Human Services, Centers for Disease Control and Prevention.
- Yiqun Chen, Haiwen Gui, Hanqi Yao, Joel Adu-Brimpong, Sigi Javitz, Val Golovko, et al. Single-lesion skin cancer risk stratification triage pathway. *JAMA Dermatology*, 160(9):972–976, 2024. doi: 10.1001/jamadermatol.2024.1832.
- Yiqun T Chen, Sizhu Lu, Sijia Li, Moran Guo, and Shengyi Li. Unifying debiasing methods for llm-as-a-judge evaluations. *arXiv preprint arXiv:2601.05420*, 2026.
- Wei-Lin Chiang, Lianmin Zheng, Ying Sheng, Anastasios Nikolas Angelopoulos, Tianle Li, Dacheng Li, et al. Chatbot arena: An open platform for evaluating llms by human preference. In *Forty-first International Conference on Machine Learning*, 2024.
- Roxana Daneshjou, Kailas Vodrahalli, Roberto A. Novoa, Melissa Jenkins, Weixin Liang,

- Veronica Rotemberg, et al. Disparities in dermatology AI performance on a diverse, curated clinical image set. *Science Advances*, 8(32):eabq6147, 2022. doi: 10.1126/sciadv.abq6147.
- Naoki Egami, Musashi Hinck, Brandon Stewart, and Hanying Wei. Using imperfect surrogates for downstream inference: Design-based supervised learning for social science applications of large language models. *Advances in Neural Information Processing Systems*, 36:68589–68601, 2023.
- Naoki Egami, Musashi Hinck, Brandon M Stewart, and Hanying Wei. Using large language model annotations for the social sciences: A general framework of using predicted variables in downstream analyses. *arXiv preprint arXiv:2404.11116*, 2024.
- Edgar Erdfelder, Franz Faul, and Axel Buchner. Gpower: A general power analysis program. *Behavior Research Methods, Instruments, & Computers*, 28(1):1–11, 1996.
- Franz Faul, Edgar Erdfelder, Albert-Georg Lang, and Axel Buchner. G\*power 3: A flexible statistical power analysis program for the social, behavioral, and biomedical sciences. *Behavior Research Methods*, 39(2):175–191, 2007.
- Jessica Gronsbell, Jianhui Gao, Yaqi Shi, Zachary R McCaw, and David Cheng. Another look at inference after prediction. *arXiv preprint arXiv:2411.19908*, 2024. Preprint.
- Wenlong Ji, Lihua Lei, and Tijana Zrnica. Predictions as surrogates: Revisiting surrogate outcomes in the age of ai. *arXiv preprint arXiv:2501.09731*, 2025.
- Pranav Mani, Peng Xu, Zachary C Lipton, and Michael Oberst. No free lunch: Non-asymptotic analysis of prediction-powered inference. *arXiv preprint arXiv:2505.20178*, 2025.
- Jiacheng Miao, Xinran Miao, Yixuan Wu, Jiwei Zhao, and Qiongshi Lu. Assumption-lean and data-adaptive post-prediction inference. *Journal of Machine Learning Research*, 26(179):1–31, 2025.
- Pierre-Emmanuel Poulet, Maylis Tran, Sophie Tezenas du Montcel, Bruno Dubois, Stanley Durrleman, and Bruno Jedynek. Prediction-powered inference for clinical trials: application to linear covariate adjustment. *BMC Medical Research Methodology*, 25(1):204, 2025.
- Alec Radford, Jong Wook Kim, Chris Hallacy, Aditya Ramesh, Gabriel Goh, Sandhini Agarwal, et al. Learning transferable visual models from natural language supervision. In *Proceedings of the 38th International Conference on Machine Learning*, volume 139 of *Proceedings of Machine Learning Research*, pages 8748–8763. PMLR, 2021. URL <https://proceedings.mlr.press/v139/radford21a.html>.
- Marc Rodger, Tim Ramsay, and Dean Fergusson. Diagnostic randomized controlled trials: the final frontier. *Trials*, 13(1):137, 2012.
- Veronica Rotemberg, Nicholas Kurtansky, Brigid Betz-Stablein, Liam Caffery, Emmanouil

- Chousakos, Noel Codella, et al. A patient-centric dataset of images and metadata for identifying melanomas using clinical context. *Scientific Data*, 8(1):34, 2021.
- Stephen Salerno, Jiacheng Miao, Awan Afiaz, Kentaro Hoffman, Anna Neufeld, Qiongshi Lu, et al. ipd: an r package for conducting inference on predicted data. *Bioinformatics*, 41(2): btaf055, 2025.
- Yilin Song, Dan M Kluger, Harsh Parikh, and Tian Gu. Demystifying prediction powered inference. *arXiv preprint arXiv:2601.20819*, 2026.
- Sonnet Xu, Haiwen Gui, Veronica Rotemberg, Tongzhou Wang, Yiqun T. Chen, and Roxana Daneshjou. A framework for evaluating the efficacy of foundation embedding models in healthcare. *medRxiv*, 2024. doi: 10.1101/2024.04.17.24305983.
- Zichun Xu, Daniela Witten, and Ali Shojaie. A unified framework for semiparametrically efficient semi-supervised learning. *arXiv preprint arXiv:2502.17741*, 2025.
- Tijana Zrnic and Emmanuel J Candès. Cross-prediction-powered inference. *Proceedings of the National Academy of Sciences*, 121(15):e2322083121, 2024.

# Supplementary Material

for

## Power Analysis for Prediction-Powered Inference

### A Supplementary Material

#### A.1 Proofs for Sections 2.2–4.1

We collect the proofs for the one-sample, two-sample, paired, and  $2 \times 2$  results stated in the main text, together with the cross-fitting extension. For clarity, each proof subsection is labeled by the result it proves. The regression-contrast derivations and the proof of Proposition 8 appear in Appendix A.4.

##### A.1.1 One-Sample Mean Results

**Proof of Proposition 1 (Mean PPI/PPI++ Variance)** This proof covers both the PPI and PPI++ variance results stated in Proposition 1.

Write

$$\widehat{\theta}_{\text{PPI}} = \bar{f}_U + (\bar{Y}_L - \bar{f}_L), \quad \widehat{\theta}_\lambda = \bar{Y}_L + \lambda(\bar{f}_U - \bar{f}_L),$$

where  $\bar{f}_U = N^{-1} \sum_{j=1}^N \widetilde{f}_j$ ,  $\bar{f}_L = n^{-1} \sum_{i=1}^n f_i$ , and  $\bar{Y}_L = n^{-1} \sum_{i=1}^n Y_i$ . Because the labeled and unlabeled splits are independent and drawn from the same covariate distribution,

$$\mathbb{E}[\bar{f}_U] = \mathbb{E}[\bar{f}_L] = \mathbb{E}[f(X)],$$

so

$$\mathbb{E}[\widehat{\theta}_{\text{PPI}}] = \mathbb{E}[f(X)] + \mathbb{E}[Y - f(X)] = \theta^*, \quad \mathbb{E}[\widehat{\theta}_\lambda] = \theta^*$$

for every fixed  $\lambda$ .

For vanilla PPI, independence of the labeled and unlabeled terms gives

$$\text{Var}(\widehat{\theta}_{\text{PPI}}) = \text{Var}(\bar{f}_U) + \text{Var}(\bar{Y}_L - \bar{f}_L) = \frac{\sigma_f^2}{N} + \frac{\sigma_\varepsilon^2}{n},$$

which is (5).

For PPI++,

$$\text{Var}(\widehat{\theta}_\lambda) = \text{Var}(\bar{Y}_L) + \lambda^2 \text{Var}(\bar{f}_U - \bar{f}_L) + 2\lambda \text{Cov}(\bar{Y}_L, \bar{f}_U - \bar{f}_L).$$

Now  $\text{Var}(\bar{Y}_L) = \sigma_Y^2/n$ ,  $\text{Var}(\bar{f}_U - \bar{f}_L) = \sigma_f^2/N + \sigma_f^2/n$ , and  $\text{Cov}(\bar{Y}_L, \bar{f}_U) = 0$  by split independence, while  $\text{Cov}(\bar{Y}_L, \bar{f}_L) = \text{Cov}(Y, f)/n$ . Substituting these identities yields

$$\text{Var}(\widehat{\theta}_\lambda) = \frac{\sigma_Y^2}{n} + \lambda^2 \left( \frac{\sigma_f^2}{N} + \frac{\sigma_f^2}{n} \right) - \frac{2\lambda \text{Cov}(Y, f)}{n},$$

which is (7). Joint asymptotic normality follows from the multivariate central limit theorem applied to the labeled and unlabeled sample means.

**Justification of the Classical Power Approximation** Under the alternative  $\theta^* = \theta_0 + \Delta$ , the classical Wald statistic is asymptotically normal with mean  $\Delta/(\sigma_Y/\sqrt{n})$  and variance 1, so the exact two-sided normal approximation is (3). The second term in that display,

$$\Phi\left(-z_{1-\alpha/2} - \frac{|\Delta|}{\sigma_Y/\sqrt{n}}\right),$$

is always no larger than the first and becomes negligible once the noncentrality  $|\Delta|/(\sigma_Y/\sqrt{n})$  is moderate. Dropping it yields the usual planning approximation  $|\Delta|/(\sigma_Y/\sqrt{n}) \geq z_{1-\alpha/2} + z_{1-\beta}$ , or equivalently  $\sigma_Y^2/n \leq S^2$ , which is the inversion used in the main text.

**Proof of Equations (8) and (9)** Given (7),

$$g(\lambda) = \text{Var}(\hat{\theta}_\lambda) = \frac{\sigma_Y^2}{n} + \lambda^2 \left( \frac{\sigma_f^2}{N} + \frac{\sigma_f^2}{n} \right) - \frac{2\lambda \text{Cov}(Y, f)}{n}.$$

This is a convex quadratic in  $\lambda$ , so its minimizer satisfies

$$g'(\lambda) = 2\lambda \left( \frac{\sigma_f^2}{N} + \frac{\sigma_f^2}{n} \right) - \frac{2\text{Cov}(Y, f)}{n} = 0.$$

Solving gives

$$\lambda^* = \frac{\text{Cov}(Y, f)}{\sigma_f^2(1 + n/N)} = \frac{\text{Cov}(Y, f)}{(1 + r)\sigma_f^2},$$

which is (8). Substituting this value back into (7) yields

$$\text{Var}(\hat{\theta}_{\lambda^*}) = \frac{\sigma_Y^2}{n} - \frac{\text{Cov}(Y, f)^2}{\sigma_f^2} \cdot \frac{N}{n(n + N)},$$

which is (9).

**Proof of Proposition 2 (PPI++ Power)** Under  $\theta^* = \theta_0 + \Delta$ ,

$$Z = \frac{\hat{\theta}_{\lambda^*} - \theta_0}{\sqrt{\text{Var}(\hat{\theta}_{\lambda^*})}} \sim \mathcal{N} \left( \frac{\Delta}{\sqrt{\text{Var}(\hat{\theta}_{\lambda^*})}}, 1 \right),$$

so the two-sided rejection probability is

$$P(|Z| \geq z_{1-\alpha/2}) = \Phi\left(-z_{1-\alpha/2} + \frac{|\Delta|}{\sqrt{\text{Var}(\hat{\theta}_{\lambda^*})}}\right) + \Phi\left(-z_{1-\alpha/2} - \frac{|\Delta|}{\sqrt{\text{Var}(\hat{\theta}_{\lambda^*})}}\right),$$

which is exactly (10).

**Proof of Proposition 3 (Sample Size Inversion)** From Proposition 2, achieving target power is ensured by

$$\text{Var}(\hat{\theta}_{\lambda^*}) \leq S^2, \quad S^2 = \frac{\Delta^2}{(z_{1-\alpha/2} + z_{1-\beta})^2}.$$

Substituting (9) gives

$$\frac{\sigma_Y^2}{n} - \frac{\text{Cov}(Y, f)^2}{\sigma_f^2} \cdot \frac{N}{n(n+N)} \leq S^2.$$

Multiplying by  $n(n+N) > 0$  and using  $\rho_{Yf}^2 = \text{Cov}(Y, f)^2 / (\sigma_Y^2 \sigma_f^2)$  yields

$$S^2 n^2 + (S^2 N - \sigma_Y^2) n - N \sigma_Y^2 (1 - \rho_{Yf}^2) \geq 0.$$

Since this quadratic opens upward, the feasible region is  $n$  greater than or equal to its positive root:

$$n \geq \frac{\sigma_Y^2 - S^2 N + \sqrt{(\sigma_Y^2 - S^2 N)^2 + 4S^2 N \sigma_Y^2 (1 - \rho_{Yf}^2)}}{2S^2},$$

which is (11).

**Proof of Corollary 4 (Rule of Thumb)** When  $N \gg n$ , we have  $N/(n + N) = 1 + o(1)$

and therefore

$$\text{Var}(\widehat{\theta}_{\lambda^*}) = \frac{\sigma_Y^2}{n} - \frac{\text{Cov}(Y, f)^2}{\sigma_f^2} \cdot \frac{1 + o(1)}{n} = \frac{\sigma_Y^2(1 - \rho_{Yf}^2)}{n} + o(n^{-1}).$$

The classical variance is  $\sigma_Y^2/n$ , so to first order the required labeled sample size scales by the same factor, giving  $n_{\text{PPI}}/n_{\text{cl}} \approx 1 - \rho_{Yf}^2$ .

### A.1.2 Two-Sample, Paired, and Contingency-Table Extensions

**Proof of Proposition 5 (Two-Sample Variance)** From the definition (12),

$$\widehat{\Delta}_{\text{PPI}} = \widehat{\theta}_{A,\text{PPI}} - \widehat{\theta}_{B,\text{PPI}}.$$

Applying the one-sample oracle-variance formula (9) within each group gives

$$\text{Var}(\widehat{\theta}_{g,\lambda_g^*}) = \frac{\sigma_{Y,g}^2}{n_g} - \frac{\text{Cov}(Y_g, f_g)^2}{\sigma_{f,g}^2} \cdot \frac{N_g}{n_g(n_g + N_g)}, \quad g \in \{A, B\}.$$

Because the two groups are independent, the cross-covariance vanishes, so

$$\text{Var}(\widehat{\Delta}_{\text{PPI}}) = \text{Var}(\widehat{\theta}_{A,\lambda_A^*}) + \text{Var}(\widehat{\theta}_{B,\lambda_B^*}),$$

which is exactly (13). The approximation (14) follows from  $\text{Cov}(Y_g, f_g)^2/\sigma_{f,g}^2 = \sigma_{Y,g}^2 \text{Corr}(Y_g, f_g)^2$

and  $N_g/(n_g + N_g) = 1 + O(n_g/N_g)$ .

**Proof of Proposition 6 (Paired Variance)** Let  $D = Y^A - Y^B$  and  $G = f^A - f^B$ . The paired PPI++ estimator is exactly the one-sample PPI++ estimator applied to the paired differences, with target parameter  $\mathbb{E}[D]$  and surrogate  $G$ . Proposition 1 therefore gives

$$\text{Var}(\widehat{\Delta}_{\text{PPI++}}) = \frac{\text{Var}(D)}{n} - \frac{\text{Cov}(D, G)^2}{\text{Var}(G)} \cdot \frac{N}{n(n+N)}.$$

Rewriting  $\text{Cov}(D, G)^2/\text{Var}(G) = \text{Var}(D)\text{Corr}(D, G)^2$  gives the equivalent form in the proposition, and letting  $N \gg n$  yields the displayed approximation.

**Proof of Proposition 7 ( $2 \times 2$  Sample Size)** For each group  $g \in \{0, 1\}$ , the event-rate estimator

$$\widehat{p}_{g, \lambda_g} = \bar{Y}_{L,g} + \lambda_g(\bar{f}_{U,g} - \bar{f}_{L,g})$$

is a one-sample PPI++ estimator for the binary mean  $p_g$ . Since  $Y_g \in \{0, 1\}$ ,  $\text{Var}(Y_g) = p_g(1 - p_g)$ , and in the regime  $N_g \gg n_g$ , Corollary 4 gives

$$\text{Var}(\widehat{p}_{g, \lambda_g^*}) \approx \frac{p_g(1 - p_g)(1 - \rho_g^2)}{n_g}.$$

For  $\log(\text{RR}) = \log p_1 - \log p_0$ , the gradient with respect to  $(p_0, p_1)$  is  $(-1/p_0, 1/p_1)^\top$ .

Since the two groups are independent, the delta method yields

$$\text{Var}(\log \widehat{\text{RR}}) \approx \frac{\text{Var}(\widehat{p}_{0, \lambda_0^*})}{p_0^2} + \frac{\text{Var}(\widehat{p}_{1, \lambda_1^*})}{p_1^2} = \frac{1}{n_0} \frac{(1 - p_0)(1 - \rho_0^2)}{p_0} + \frac{1}{n_1} \frac{(1 - p_1)(1 - \rho_1^2)}{p_1}.$$

Substituting  $n_1 = \kappa n_0$  gives the first displayed variance formula in the proposition.

For  $\log(\text{OR}) = \text{logit}(p_1) - \text{logit}(p_0)$ , the gradient is  $(-[p_0(1 - p_0)]^{-1}, [p_1(1 - p_1)]^{-1})^\top$ , so

the same argument gives

$$\text{Var}(\log \widehat{\text{OR}}) \approx \frac{1}{n_0} \frac{1 - \rho_0^2}{p_0(1 - p_0)} + \frac{1}{n_1} \frac{1 - \rho_1^2}{p_1(1 - p_1)}.$$

The sample-size expressions follow by imposing  $\text{Var}(\log \widehat{\text{RR}}) \leq S_{\text{RR}}^2$  and  $\text{Var}(\log \widehat{\text{OR}}) \leq S_{\text{OR}}^2$  and then solving for  $n_0$ ; the balanced-design formulas set  $\kappa = 1$ . Setting  $\rho_0 = \rho_1 = 0$  recovers the usual classical formulas.

### A.1.3 Cross-Fitted PPI++ Distribution

We state the cross-fitting result directly for the one-sample mean problem of Sections 2.2–3.

Partition the labeled sample into folds  $I_1, \dots, I_K$ , let  $f^{(j)}$  denote the predictor trained without fold  $I_j$ , and define the cross-fitted PPI++ estimator

$$\widehat{\theta}_{\lambda, \text{cf}} = \bar{Y}_L + \lambda \left( \frac{1}{K} \sum_{j=1}^K \bar{f}_U^{(j)} - \frac{1}{n} \sum_{j=1}^K \sum_{i \in I_j} f^{(j)}(X_i) \right), \quad \bar{f}_U^{(j)} = \frac{1}{N} \sum_{m=1}^N f^{(j)}(\tilde{X}_m).$$

This is the same rectified mean estimator as in (6), except that each labeled observation is evaluated by a predictor that was not trained on its own fold.

**Assumption 1 (Prediction stability)** *The predictors  $f^{(1)}, \dots, f^{(K)}$  trained on the  $K$  folds satisfy  $\|f^{(j)} - \bar{f}\|_2 = o_P(1)$  as  $n \rightarrow \infty$ , where  $\bar{f} = K^{-1} \sum_{j=1}^K f^{(j)}$  is the average predictor.*

Lemmas 3–4 in the proof of Theorem 2 of [Zrnic and Candès \[2024\]](#), specialized to the scalar mean estimating function  $\ell_\theta(Y, X) = Y - \theta$ , imply that the fold-specific prediction averages can be replaced by the average predictor  $\bar{f}$  without affecting the estimator at the

$n^{-1/2}$  scale:

$$\begin{aligned}\frac{1}{K} \sum_{j=1}^K \bar{f}_U^{(j)} &= \frac{1}{N} \sum_{m=1}^N \bar{f}(\tilde{X}_m) + o_P(n^{-1/2}), \\ \frac{1}{n} \sum_{j=1}^K \sum_{i \in I_j} f^{(j)}(X_i) &= \frac{1}{n} \sum_{i=1}^n \bar{f}(X_i) + o_P(n^{-1/2}).\end{aligned}$$

Therefore

$$\hat{\theta}_{\lambda, \text{cf}} = \bar{Y}_L + \lambda(\bar{f}_{U, \bar{f}} - \bar{f}_{L, \bar{f}}) + o_P(n^{-1/2}),$$

where

$$\bar{f}_{U, \bar{f}} = \frac{1}{N} \sum_{m=1}^N \bar{f}(\tilde{X}_m), \quad \bar{f}_{L, \bar{f}} = \frac{1}{n} \sum_{i=1}^n \bar{f}(X_i).$$

Conditional on the limiting predictor  $\bar{f}$ , this is exactly the same algebraic form as the fixed-predictor estimator in (6), with  $f$  replaced by  $\bar{f}$ . Since the labeled and unlabeled samples are independent, the multivariate central limit theorem gives

$$\sqrt{n}(\hat{\theta}_{\lambda, \text{cf}} - \theta^*) \xrightarrow{d} \mathcal{N}\left(0, \sigma_Y^2 + \lambda^2(1+r)\sigma_{\bar{f}}^2 - 2\lambda \text{Cov}(Y, \bar{f})\right),$$

where  $r = \lim n/N$  and  $\sigma_{\bar{f}}^2 = \text{Var}(\bar{f}(X))$ . Equivalently,

$$\text{Var}(\hat{\theta}_{\lambda, \text{cf}}) = \frac{\sigma_Y^2}{n} + \lambda^2 \sigma_{\bar{f}}^2 \left(\frac{1}{n} + \frac{1}{N}\right) - \frac{2\lambda \text{Cov}(Y, \bar{f})}{n} + o(n^{-1}).$$

The oracle choice in this cross-fitted setting is therefore

$$\lambda_{\text{cf}}^* = \frac{\text{Cov}(Y, \bar{f})}{(1+r)\sigma_{\bar{f}}^2},$$

and substituting it into the variance expression yields the same first-order formula as (9), again with  $f$  replaced by the limiting predictor  $\bar{f}$ .

## A.2 Supplementary Simulation Results

**Head-to-head planning comparison.** Table S1 reorganizes representative results from the main simulation settings into a single comparison across one-sample, two-sample, and paired continuous designs. It does not introduce a new setting; rather, it summarizes the practical tradeoffs between classical inference, vanilla PPI, and PPI++ (oracle and plugin) using common planning targets.

Table S1: Head-to-head comparison across representative continuous planning scenarios (one-sample:  $\Delta = 0.2$ ; two-sample:  $\Delta = 0.3$ ; paired:  $\Delta = 0.3$ ; all with  $N = 5000$ ,  $\rho = 0.7$ , target power 0.80,  $\alpha = 0.05$ ; MC  $R = 5000$ ). For plugin PPI++, planning uses the oracle closed-form  $n$  and evaluates performance with plugin  $\hat{\lambda}$ .

Design	Method	Required $n$	Achieved power	Type I error	Reduction
One-sample	Classical	197	0.797	0.048	0.0%
One-sample	Vanilla PPI	123	0.801	0.052	37.6%
One-sample	PPI++ (Oracle)	102	0.811	0.048	48.2%
One-sample	PPI++ (Plugin)	102	0.804	0.056	48.2%
Two-sample	Classical	175	0.796	0.046	0.0%
Two-sample	Vanilla PPI	109	0.791	0.048	37.7%
Two-sample	PPI++ (Oracle)	91	0.800	0.054	48.0%
Two-sample	PPI++ (Plugin)	91	0.808	0.050	48.0%
Paired	Classical	88	0.801	0.050	0.0%
Paired	Vanilla PPI	54	0.810	0.054	38.6%
Paired	PPI++ (Oracle)	45	0.802	0.049	48.9%
Paired	PPI++ (Plugin)	45	0.805	0.055	48.9%

## A.3 Additional Application Summary

Table S2 collects representative design points from the three real-data applications in Section 6.

Table S2: Representative planning outputs and held-out achieved power from the 15% pilot / 60% held-out workflow. The Baron row uses the beta-minus-alpha composition contrast at  $N = 500$ ; NHANES uses mean systolic blood pressure at  $N = 2,000$ ; and ISIC uses melanoma prevalence at  $N = 10,000$ .

Application	Surrogate	$\rho_{Yf}^2$	$\Delta$	$n^*$	Achieved power	Reduction
Baron	Classical	—	0.10	785	0.840	—
Baron	Donor GLM	0.141	0.10	740	0.826	6%
Baron	INS GLM	0.967	0.10	325	0.826	59%
Baron	Top-20 RF	0.983	0.10	306	0.840	61%
NHANES	Classical	—	4 mmHg	187	0.830	—
NHANES	Age-only LM	0.218	4 mmHg	149	0.836	20%
NHANES	Clinical LM	0.244	4 mmHg	144	0.848	23%
NHANES	Clinical RF	0.258	4 mmHg	142	0.812	24%
ISIC	Classical	—	0.01	1,334	0.806	—
ISIC	Metadata GLM	0.030	0.01	1,299	0.868	3%
ISIC	Thumbnail PCA GLM	0.020	0.01	1,310	0.872	2%
ISIC	CLIP GLM	0.032	0.01	1,296	0.832	3%

## A.4 Regression and GLM Extensions

This single appendix subsection collects the OLS and GLM contrast derivations together with the proof of Proposition 8. It supports the main-text regression subsection rather than introducing a separate appendix module, and uses the same contrast-level notation  $(V_{YY}, V_{ff}, V_{Yf})$  as the main text. These derivations are validated by the Monte Carlo regression-contrast experiments in Section 5.2.

**Linear Regression (OLS).** Consider the population least-squares target

$$\beta^* = \arg \min_{\beta \in \mathbb{R}^p} \mathbb{E}[(Y - X^\top \beta)^2].$$

Its first-order condition is

$$\mathbb{E}[X\{Y - X^\top \beta^*\}] = 0,$$

or equivalently

$$\mathbb{E}[XX^\top]\beta^* = \mathbb{E}[XY].$$

Let

$$\Sigma_{XX} := \mathbb{E}[XX^\top].$$

When  $\Sigma_{XX}$  is nonsingular,  $\beta^* = \Sigma_{XX}^{-1}\mathbb{E}[XY]$ .

With an external predictor  $f(X)$ , we can decompose

$$\mathbb{E}[XY] = \mathbb{E}[Xf(X)] + \mathbb{E}[X\{Y - f(X)\}],$$

which leads to the empirical PPI estimator

$$\hat{\beta}_{\text{PPI}} = \hat{\Sigma}_{XX,U}^{-1} \left[ \frac{1}{N} \sum_{j=1}^N \tilde{X}_j \tilde{f}_j + \frac{1}{n} \sum_{i=1}^n X_i \{Y_i - f_i\} \right],$$

where

$$\hat{\Sigma}_{XX,U} = \frac{1}{N} \sum_{j=1}^N \tilde{X}_j \tilde{X}_j^\top.$$

For a contrast  $\theta = a^\top \beta$ , define the OLS score residuals

$$\psi_Y(X, Y) = X\{Y - X^\top \beta^*\}, \quad \psi_f(X) = X\{f(X) - X^\top \beta^*\},$$

and the corresponding covariance blocks

$$\Sigma_{YY} = \text{Var}\{\psi_Y(X, Y)\}, \quad \Sigma_{ff} = \text{Var}\{\psi_f(X)\}, \quad \Sigma_{Yf} = \text{Cov}\{\psi_Y(X, Y), \psi_f(X)\}.$$

The contrast-level quantities used in the main text are then

$$V_{YY}^{\text{OLS}} = a^\top \Sigma_{XX}^{-1} \Sigma_{YY} \Sigma_{XX}^{-1} a,$$

$$V_{ff}^{\text{OLS}} = a^\top \Sigma_{XX}^{-1} \Sigma_{ff} \Sigma_{XX}^{-1} a,$$

$$V_{Yf}^{\text{OLS}} = a^\top \Sigma_{XX}^{-1} \Sigma_{Yf} \Sigma_{XX}^{-1} a.$$

The rectified PPI++ estimator solves

$$0 = \frac{1}{n} \sum_{i=1}^n X_i (Y_i - X_i^\top \beta) + \lambda \left[ \frac{1}{N} \sum_{j=1}^N \tilde{X}_j (\tilde{f}_j - \tilde{X}_j^\top \beta) - \frac{1}{n} \sum_{i=1}^n X_i (f_i - X_i^\top \beta) \right].$$

A first-order expansion around  $\beta^*$  gives

$$\text{Var}(a^\top \hat{\beta}_\lambda) \approx \frac{V_{YY}^{\text{OLS}} + \lambda^2(1+r)V_{ff}^{\text{OLS}} - 2\lambda V_{Yf}^{\text{OLS}}}{n}, \quad r = \frac{n}{N}.$$

The oracle tuning parameter is therefore  $\lambda^*(a) = V_{Yf}^{\text{OLS}} / \{(1+r)V_{ff}^{\text{OLS}}\}$ , and the corresponding fixed- $N$  sample-size formula is exactly the one stated in Proposition 8; Appendix A.4 contains the algebraic inversion.

**Generalized Linear Models (GLMs).** For a GLM with mean function  $\mu_\beta(X)$ , the target parameter  $\beta^*$  satisfies the score equation

$$\mathbb{E}[X\{Y - \mu_\beta(X)\}] = 0 \quad \text{at } \beta = \beta^*.$$

If  $\mu_f(X)$  is an external prediction for  $\mathbb{E}[Y | X]$ , then

$$\mathbb{E}[X\{Y - \mu_\beta(X)\}] = \mathbb{E}[X\{\mu_f(X) - \mu_\beta(X)\}] + \mathbb{E}[X\{Y - \mu_f(X)\}].$$

This yields the empirical PPI score

$$\hat{U}_{\text{PPI}}(\beta) = \frac{1}{N} \sum_{j=1}^N \tilde{X}_j (\mu_f(\tilde{X}_j) - \mu_\beta(\tilde{X}_j)) + \frac{1}{n} \sum_{i=1}^n X_i (Y_i - \mu_f(X_i)).$$

Let

$$J := -\mathbb{E} \left[ \frac{\partial}{\partial \beta} X\{Y - \mu_\beta(X)\} \Big|_{\beta=\beta^*} \right]$$

denote the Fisher information matrix. For canonical links,  $J = \mathbb{E}[w_\star(X)XX^\top]$  with the usual working weight  $w_\star(X)$  evaluated at  $\beta^\star$ .

Define the GLM score residuals

$$\phi_Y(X, Y) = X\{Y - \mu_{\beta^\star}(X)\}, \quad \phi_f(X) = X\{\mu_f(X) - \mu_{\beta^\star}(X)\},$$

their covariance blocks

$$\Sigma_{YY}^{\text{GLM}} = \text{Var}\{\phi_Y(X, Y)\}, \quad \Sigma_{ff}^{\text{GLM}} = \text{Var}\{\phi_f(X)\}, \quad \Sigma_{Yf}^{\text{GLM}} = \text{Cov}\{\phi_Y(X, Y), \phi_f(X)\},$$

and the induced contrast-level quantities

$$V_{YY}^{\text{GLM}} = a^\top J^{-1} \Sigma_{YY}^{\text{GLM}} J^{-1} a,$$

$$V_{ff}^{\text{GLM}} = a^\top J^{-1} \Sigma_{ff}^{\text{GLM}} J^{-1} a,$$

$$V_{Yf}^{\text{GLM}} = a^\top J^{-1} \Sigma_{Yf}^{\text{GLM}} J^{-1} a.$$

The rectified PPI++ score is

$$\hat{U}_\lambda(\beta) = \frac{1}{n} \sum_{i=1}^n X_i (Y_i - \mu_\beta(X_i)) + \lambda \left[ \frac{1}{N} \sum_{j=1}^N \tilde{X}_j (\mu_f(\tilde{X}_j) - \mu_\beta(\tilde{X}_j)) - \frac{1}{n} \sum_{i=1}^n X_i (\mu_f(X_i) - \mu_\beta(X_i)) \right]. \quad (15)$$

Solving (15) gives  $\hat{\beta}_\lambda$ . A one-step expansion yields

$$\text{Var}(a^\top \hat{\beta}_\lambda) \approx \frac{V_{YY}^{\text{GLM}} + \lambda^2(1+r)V_{ff}^{\text{GLM}} - 2\lambda V_{Yf}^{\text{GLM}}}{n}, \quad r = \frac{n}{N}.$$

Hence  $\lambda^*(a) = V_{Yf}^{\text{GLM}} / \{(1+r)V_{ff}^{\text{GLM}}\}$ , and the same fixed- $N$  sample-size inversion as in Proposition 8 applies with the GLM-specific contrast-level terms. For logistic regression in particular,  $J = \mathbb{E}[\mu_*(X)\{1 - \mu_*(X)\}XX^\top]$ .

**Proof of Proposition 8.** The derivations in Appendix A.4 show that for either OLS or a GLM contrast,

$$\text{Var}(\hat{\theta}_\lambda) \approx \frac{V_{YY} + \lambda^2(1+r)V_{ff} - 2\lambda V_{Yf}}{n}, \quad r = \frac{n}{N}.$$

This is a convex quadratic in  $\lambda$ , so differentiating with respect to  $\lambda$  and setting the derivative to zero gives

$$\lambda^* = \frac{V_{Yf}}{(1+r)V_{ff}}.$$

Substituting  $\lambda^*$  back into the variance expression yields

$$\text{Var}(\widehat{\theta}_{\lambda^*}) \approx \frac{1}{n} \left( V_{YY} - \frac{V_{Yf}^2}{(1+r)V_{ff}} \right) = \frac{1}{n} \left( V_{YY} - \frac{V_{Yf}^2}{V_{ff}} \cdot \frac{N}{N+n} \right).$$

For a two-sided Wald test, the same argument as in the one-sample case shows that target power is achieved whenever

$$\text{Var}(\widehat{\theta}_{\lambda^*}) \leq S^2, \quad S^2 = \frac{\Delta^2}{(z_{1-\alpha/2} + z_{1-\beta})^2}.$$

Therefore

$$\frac{1}{n} \left( V_{YY} - \frac{V_{Yf}^2}{V_{ff}} \cdot \frac{N}{N+n} \right) \leq S^2.$$

Multiplying through by  $n(N+n) > 0$  gives

$$S^2 n^2 + (S^2 N - V_{YY})n - N \left( V_{YY} - \frac{V_{Yf}^2}{V_{ff}} \right) \geq 0.$$

Since this quadratic opens upward, the feasible region is  $n$  greater than or equal to its positive root:

$$n \geq \frac{V_{YY} - S^2 N + \sqrt{(V_{YY} - S^2 N)^2 + 4S^2 N \left( V_{YY} - \frac{V_{Yf}^2}{V_{ff}} \right)}}{2S^2},$$

which is the fixed- $N$  formula in Proposition 8.

Finally, when  $N \gg n$ , we have  $N/(N + n) = 1 + o(1)$ , so

$$\text{Var}(\hat{\theta}_{\lambda^*}) \approx \frac{1}{n} \left( V_{YY} - \frac{V_{Yf}^2}{V_{ff}} \right),$$

and solving  $\text{Var}(\hat{\theta}_{\lambda^*}) \leq S^2$  gives

$$n \geq \frac{V_{YY} - V_{Yf}^2/V_{ff}}{S^2},$$

which is the large- $N$  simplification stated in the proposition.

## A.5 Additional Simulation Figures

This appendix subsection collects the supporting simulation figures that are referenced but not shown in the main text. They cover the two-sample and paired validations from Section 5.1, and the robustness checks from Section 5.3.

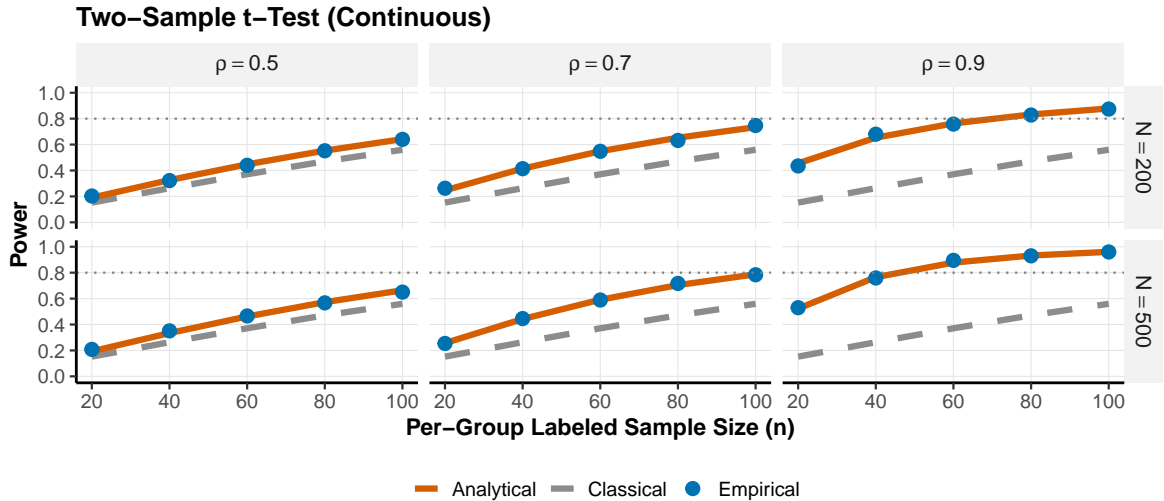


Figure S1: Two-sample  $t$ -test with continuous Gaussian outcomes. Analytical (lines) versus empirical (points) power.

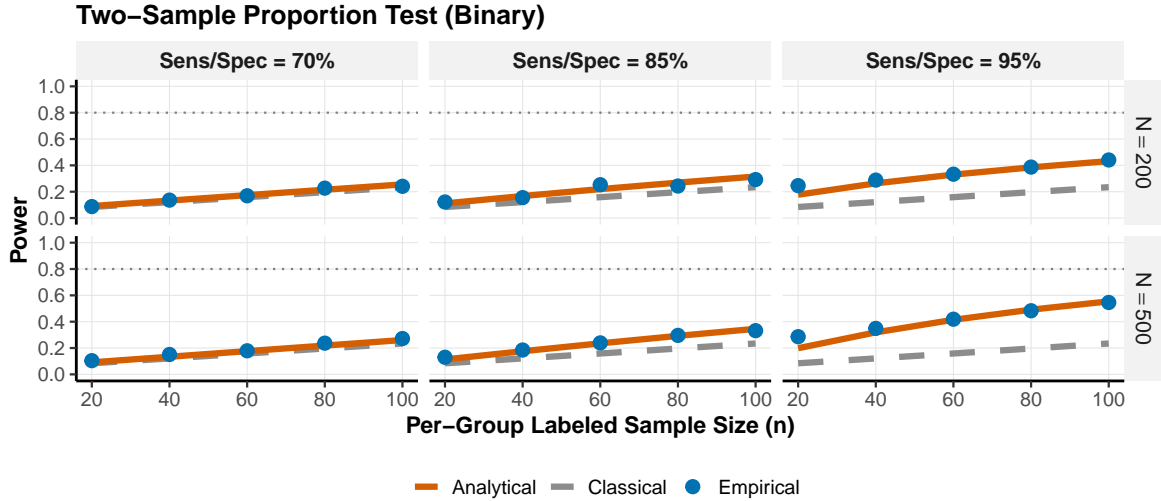


Figure S2: Two-sample proportion test with binary outcomes. Analytical (lines) versus empirical (points) power.

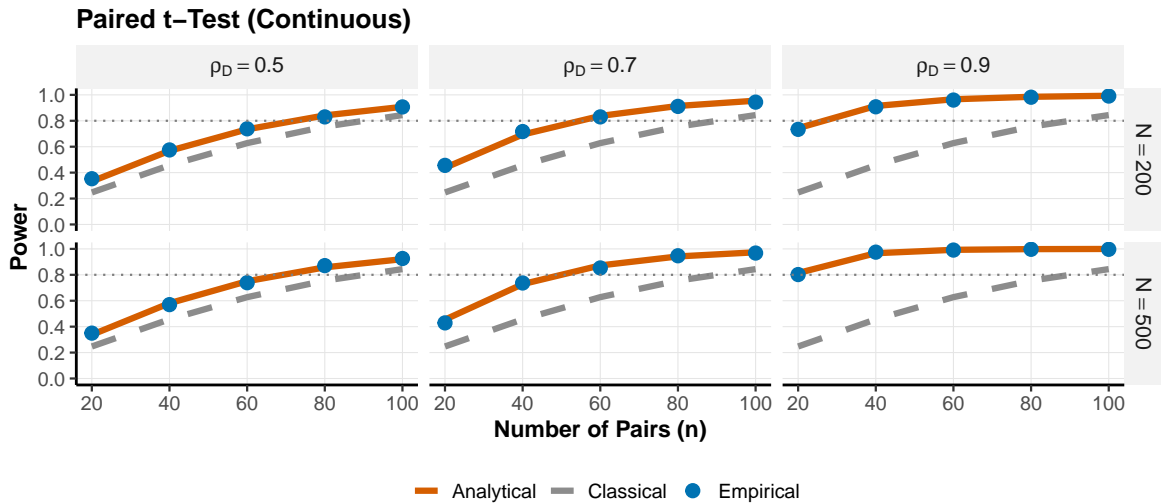


Figure S3: Paired  $t$ -test with continuous differences. Analytical (lines) versus empirical (points) power.

**Two-sample and paired settings.**

**Auxiliary planning checks.**

**Sample-size inversion.** For continuous one-sample means, binary one-sample means, continuous two-sample means, and paired continuous designs, we fix target powers in

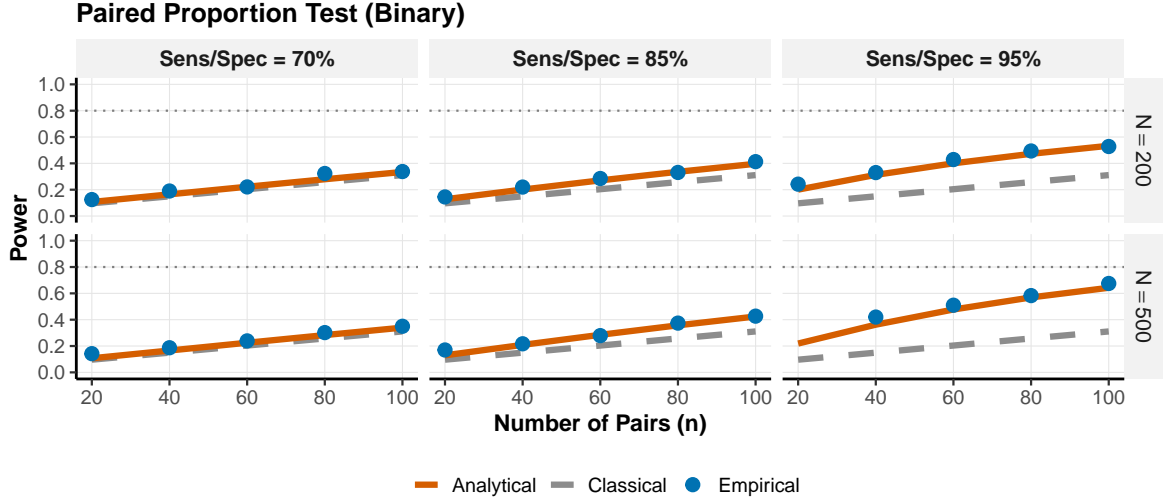


Figure S4: Paired proportion test with binary differences. Analytical (lines) versus empirical (points) power.

$\{0.60, 0.70, 0.80, 0.90\}$  and verify that the computed  $n^*$  achieves power close to the target. Figure S5 plots achieved power minus target power, so exact inversion corresponds to zero. Each point is one design configuration within a test family, such as a particular  $\rho$  or binary-surrogate accuracy, evaluated at the integer  $n^*$  returned by the planning formula. The analytical points recompute the asymptotic power at that integer  $n^*$ , while the empirical points are Monte Carlo rejection rates at the same  $n^*$ , so neither series is forced to equal the target exactly. Analytical deviations are uniformly small, while empirical deviations are somewhat larger in the smallest- $n$  configurations. Some high-power binary targets at  $N = 500$  required  $n^* > N$  under the fixed-pool convention used in the planning code and therefore do not appear.

**Rule-of-thumb validation.** We sweep  $\rho \in [0.1, 0.99]$  and  $N \in \{200, 500, 1,000, 5,000\}$ . Rather than plotting the raw ratio  $n_{\text{PPI}}/n_{\text{cl}}$ , Figure S6 shows its deviation from the rule-of-thumb approximation  $1 - \rho^2$ . The error shrinks toward zero as  $N$  grows, confirming

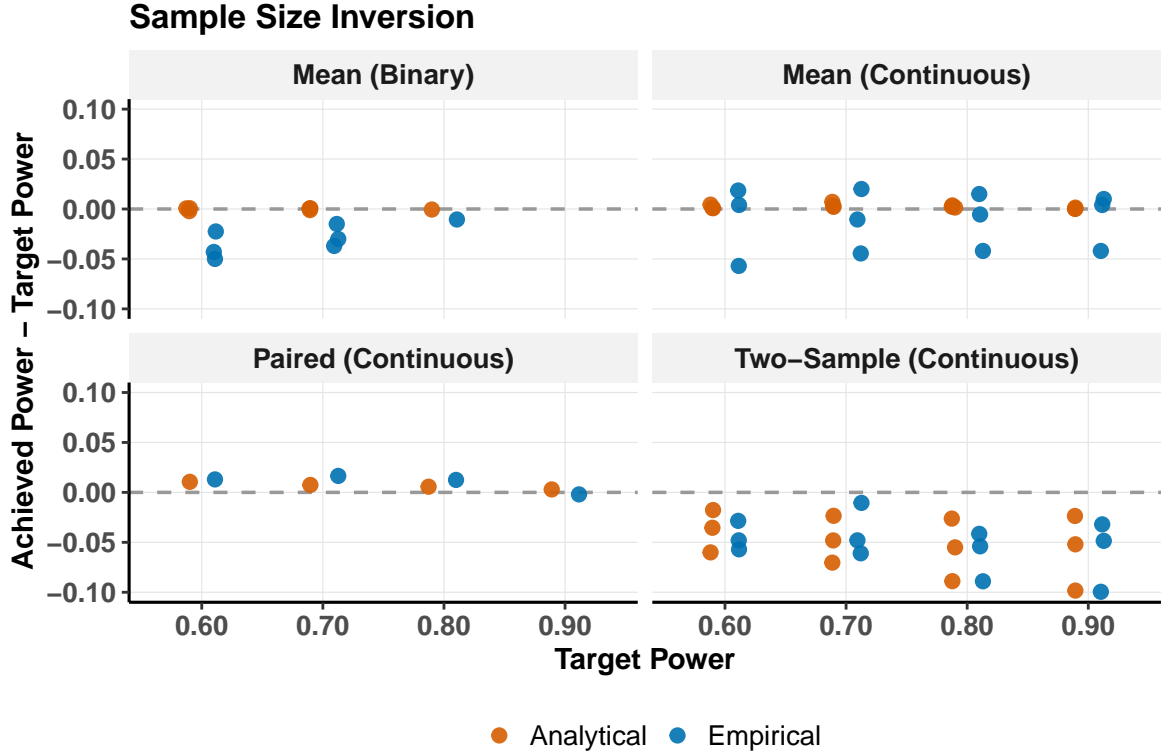


Figure S5: Sample-size inversion check across one-sample, two-sample, and paired designs. Points show achieved power minus target power at the planned integer  $n^*$ ; exact inversion would lie on the horizontal zero line.

Corollary 4.

**Type I error calibration.** We repeat the core one-sample, two-sample, paired, and distributional-robustness experiments under the null ( $\Delta = 0$ ) with  $R = 2,000$  replicates. Observed PPI++ rejection rates are close to the nominal level: continuous settings range from 0.044 to 0.061, and binary settings from 0.044 to 0.060. Figure S7 shows the continuous null settings; the binary calibration results are summarized here by their observed range.

**Plugin  $\lambda$  convergence.** We verify that the plugin estimate  $\hat{\lambda}$  (computed from labeled-data sample moments) converges to the oracle  $\lambda^*$  as  $n$  increases, with  $N = 1,000$  fixed. Figure S8 reports the root-mean-squared error of  $\hat{\lambda}$  relative to  $\lambda^*$ , which shrinks toward zero as  $n$  grows.

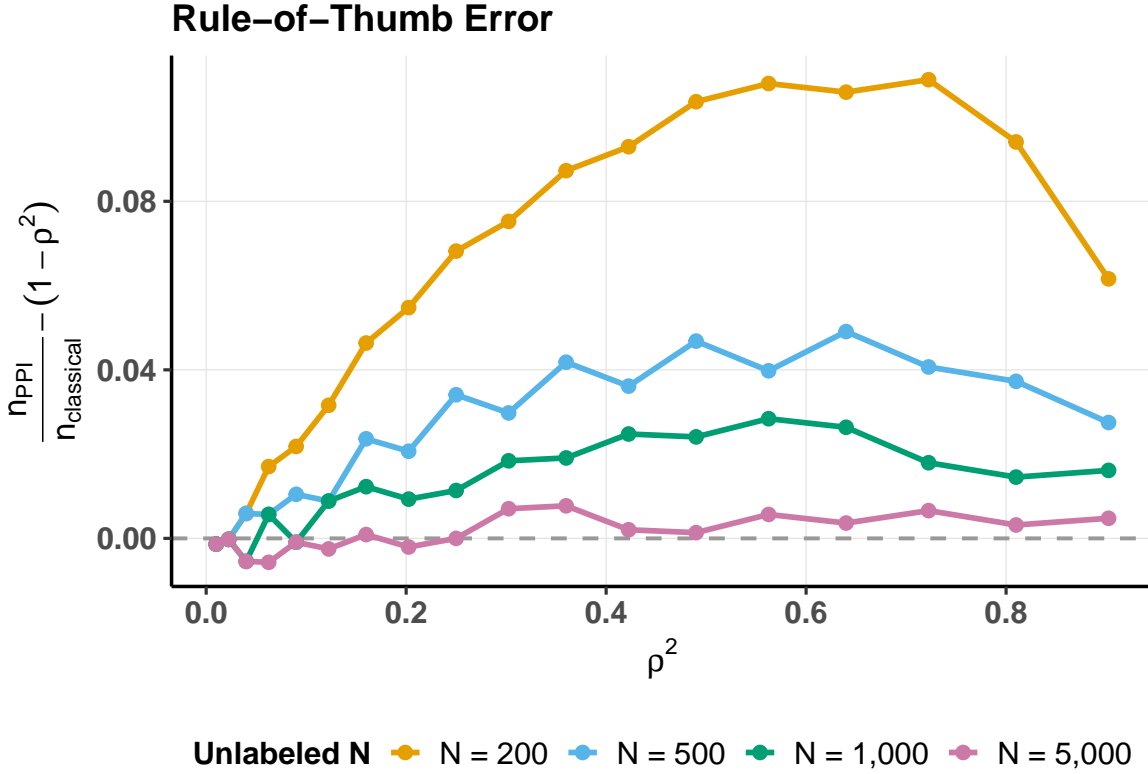


Figure S6: Rule-of-thumb error for the labeled-sample reduction ratio. Curves plot  $n_{\text{PPI}}/n_{\text{cl}} - (1 - \rho^2)$  against  $\rho^2$  for several unlabeled-sample sizes  $N$ .

### Robustness analyses.

**Plugin versus oracle  $\lambda$ .** All previous robustness plots use the oracle  $\lambda^*$  computed from the true population moments. In practice,  $\lambda$  must be estimated from data. This experiment reruns the Gaussian one-sample DGP from the main validation grid on the same  $n \in \{20, 40, 60, 80, 100\}$  and  $N \in \{200, 500\}$  grid, with both the oracle and a plugin  $\hat{\lambda}$  estimated from labeled-data covariance. Figure S9 shows that empirical power under the plugin  $\hat{\lambda}$  closely tracks the oracle empirical curve; the analytical curve (based on the oracle variance) remains a close approximation even at the smallest design point  $n = 20$ . Quantitatively, the maximum discrepancy is 0.023 for oracle  $\lambda^*$  and 0.037 for plugin  $\hat{\lambda}$ , while the maximum

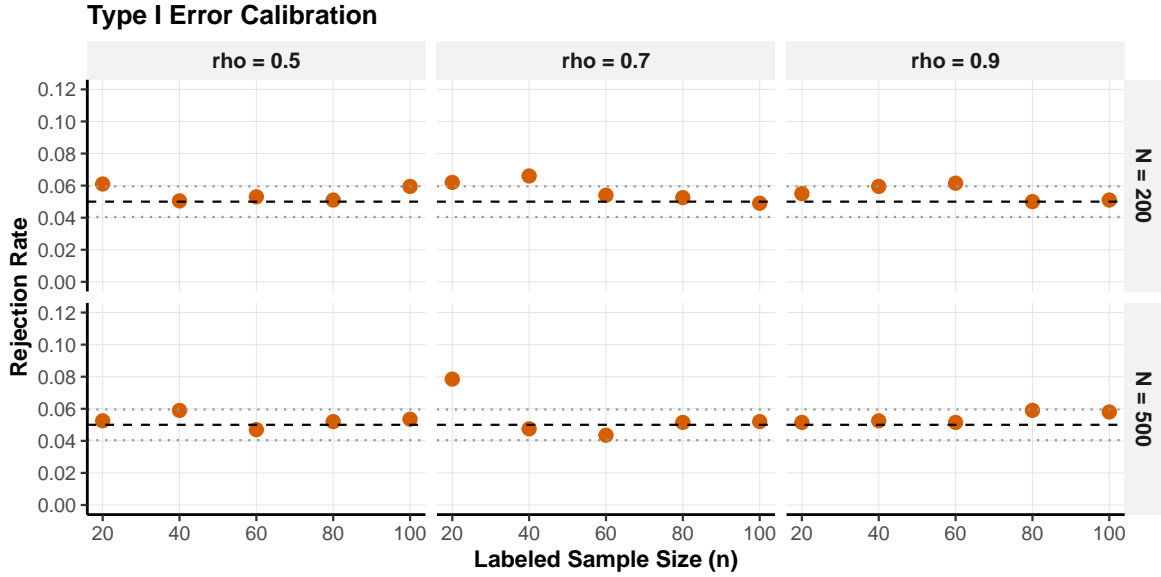


Figure S7: Type I error calibration for the continuous null settings. Rejection rates remain close to the nominal level 0.05, with dotted lines showing the corresponding Monte Carlo fluctuation band for  $R = 2,000$  replicates.

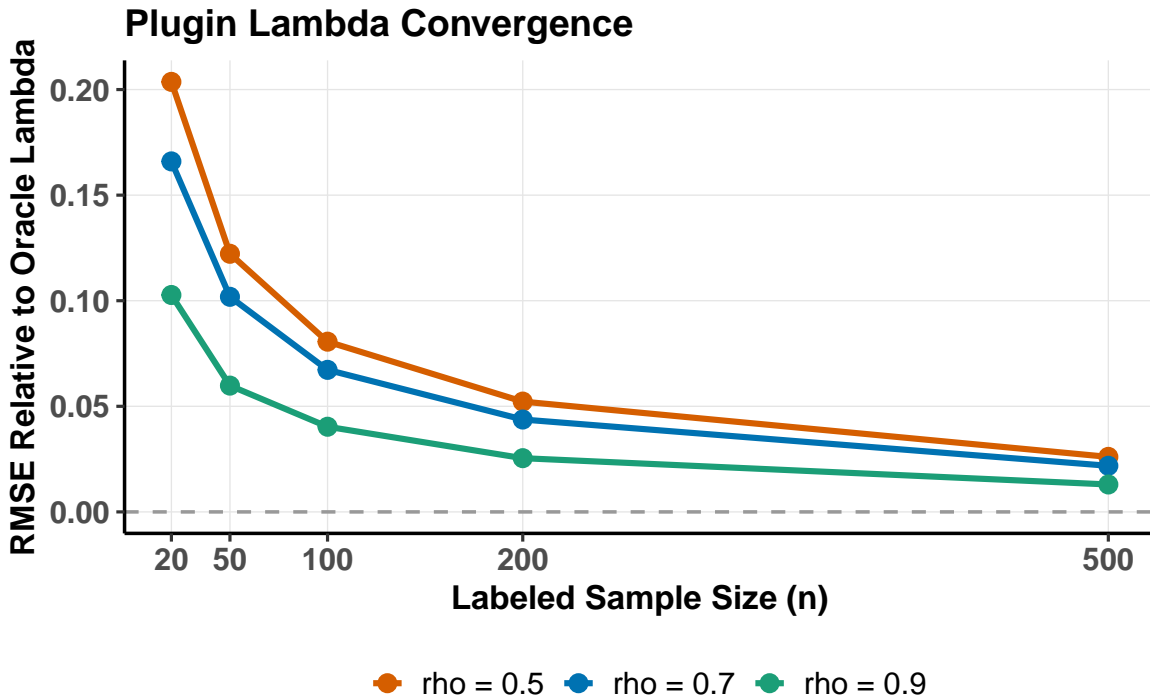


Figure S8: Convergence of the plugin  $\hat{\lambda}$  toward the oracle  $\lambda^*$  as the labeled sample size grows. The plotted quantity is the root-mean-squared error relative to the oracle tuning value.

oracle–plugin empirical difference is 0.031.

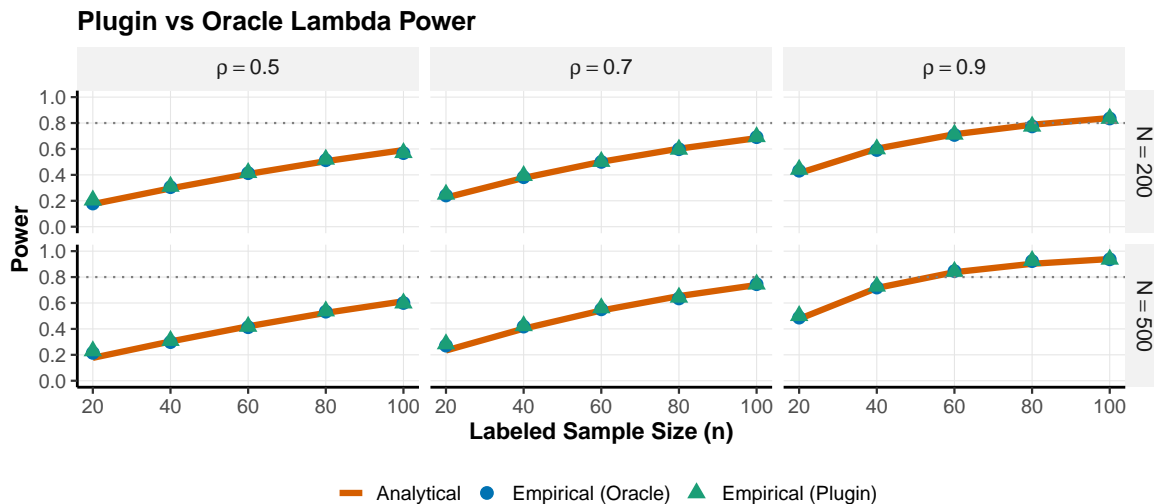


Figure S9: Power with plugin versus oracle tuning. The analytical curve uses the oracle variance formula, while the empirical points compare oracle and plugin versions of the PPI++ test.

**Power as a function of effect size.** While the main validation figures fix  $\Delta$  and vary  $n$ , it is also standard to examine power as a function of effect size at fixed sample sizes. Here we sweep  $\Delta \in [0, 0.5]$  for  $n \in \{20, 40, 60, 80, 100\}$  with  $N = 500$ . Figure S10 displays the characteristic S-shaped power curves; higher  $\rho$  shifts the curve to the left, requiring smaller  $\Delta$  to achieve any given power level. The maximum discrepancy is 0.050. This setting does not introduce a new variance formula; it simply visualizes the same one-sample planning problem as the main one-sample validation figures, but on an effect-size axis rather than a sample-size axis.

**Small labeled samples.** The power formula relies on the normal approximation, which may be inaccurate when  $n$  is very small. Here we push to  $n \in \{15, 20, 25, 30, 50, 100\}$  with  $R = 2,000$  replicates for tighter Monte Carlo estimates. Figure S11 shows that the analytical

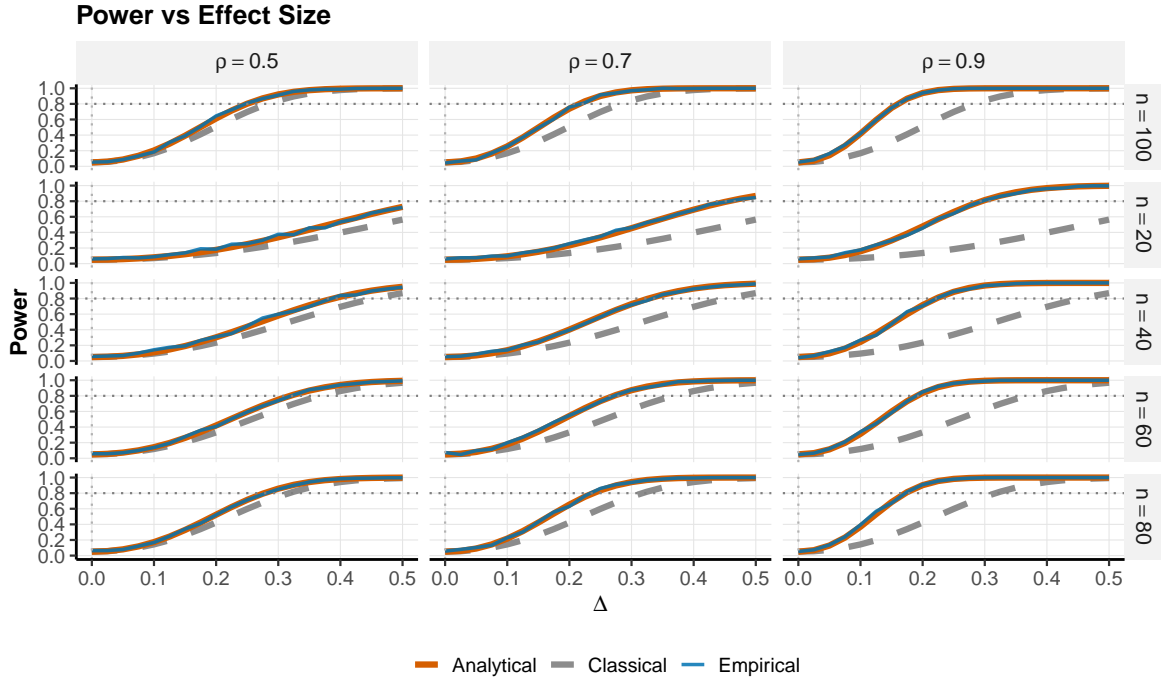


Figure S10: Power as a function of effect size for the Gaussian one-sample mean problem. Higher prediction quality shifts the PPI++ curve leftward relative to the classical design.

formula remains usable for Gaussian outcomes even at small  $n$ . The maximum discrepancy is 0.036 for  $n \leq 25$  and much smaller (0.009) for  $n \geq 50$ , suggesting that the normal approximation is most reliable once  $n$  is at least moderate.

**$N/n$  ratio sensitivity.** Current PPI practice typically assumes  $N \gg n$ . Here we fix  $n = 50$  and vary  $N/n$  from 1 to 100. Figure S12 reveals three findings. First, at  $N/n = 1$ , the PPI++ power gain is smaller than in high-ratio regimes but can still be material when  $\rho$  is high. Second, the gain saturates: most of the benefit accrues by  $N/n \approx 10$ –20. Third, the gain is modulated by  $\rho$ : at  $\rho = 0.5$ , even  $N/n = 100$  provides only a modest improvement, while at  $\rho = 0.9$ , the improvement is substantial.

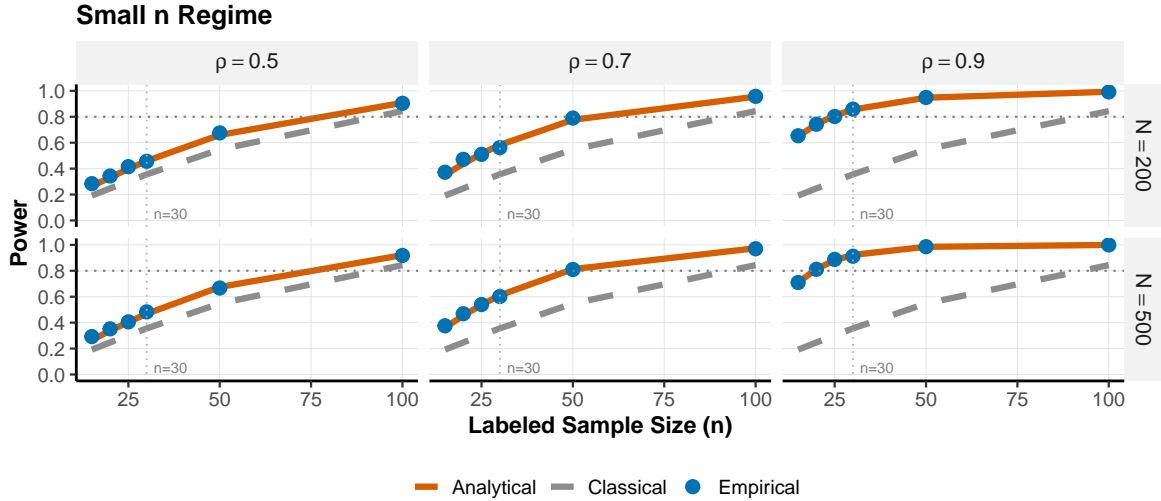


Figure S11: Small- $n$  regime for the Gaussian one-sample mean problem. Agreement remains usable down to  $n = 15$ , with the largest discrepancies concentrated in the smallest labeled samples.

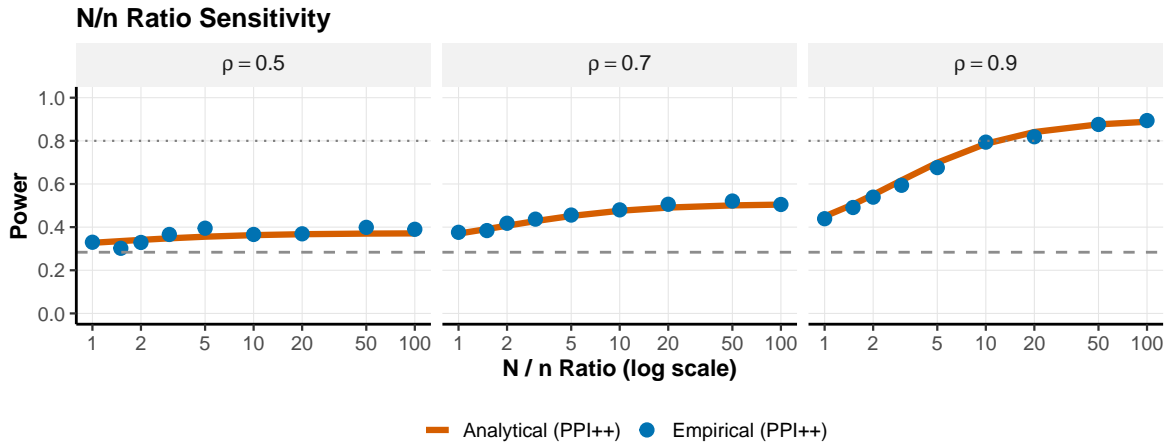


Figure S12: Sensitivity to the unlabeled-to-labeled ratio  $N/n$ . Power gains increase quickly at first and then saturate once the unlabeled pool is moderately large.

**Unequal group sizes.** Two-sample tests in practice often have unbalanced designs. Here we fix the total labeled budget ( $n_A + n_B = 100$ ,  $N_A + N_B = 600$ ) and vary the allocation ratio  $n_A : n_B \in \{1:1, 1.5:1, 2:1, 3:1, 4:1\}$ , allocating the unlabeled totals in the same ratio so that  $N_A : N_B = n_A : n_B$ . Figure S13 shows that the analytical formula accurately tracks empirical power across all ratios. Power decreases with increasing imbalance, consistent with

the classical result that balanced allocation maximizes power for a fixed total budget. The maximum discrepancy is 0.030.

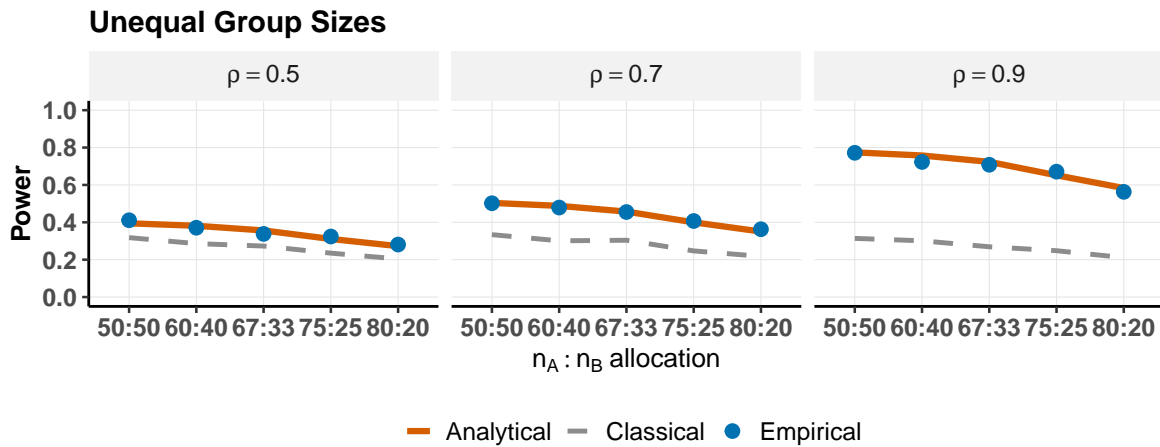


Figure S13: Unequal-group two-sample designs. Power decreases with stronger allocation imbalance, while the analytical formula continues to track the empirical results closely.

**Misspecified prediction quality.** In practice, the user must specify  $\rho_{Yf}$  at the planning stage based on pilot data or published benchmarks, but the true correlation may differ. This experiment quantifies this sensitivity: for each  $\rho_{\text{plan}} \in \{0.5, 0.7, 0.9\}$ , we compute the required  $n^*$  assuming  $\rho_{\text{plan}}$ , then evaluate the actual power at  $n^*$  under the true  $\rho_{\text{true}} = \rho_{\text{plan}} + \delta_\rho$  with  $\delta_\rho \in \{-0.20, -0.15, \dots, 0.20\}$ , retaining only feasible values with  $\rho_{\text{true}} \in (0.01, 0.99)$ , and  $R = 2,000$  replicates. When  $\rho_{\text{true}} < \rho_{\text{plan}}$  (the predictor is worse than expected), the study is underpowered. Conversely, when  $\rho_{\text{true}} > \rho_{\text{plan}}$ , the study is conservatively overpowered. This asymmetry suggests that practitioners should use conservative (lower-bound) estimates of prediction quality when planning studies, analogous to the common advice to use conservative effect-size estimates in classical power analysis.

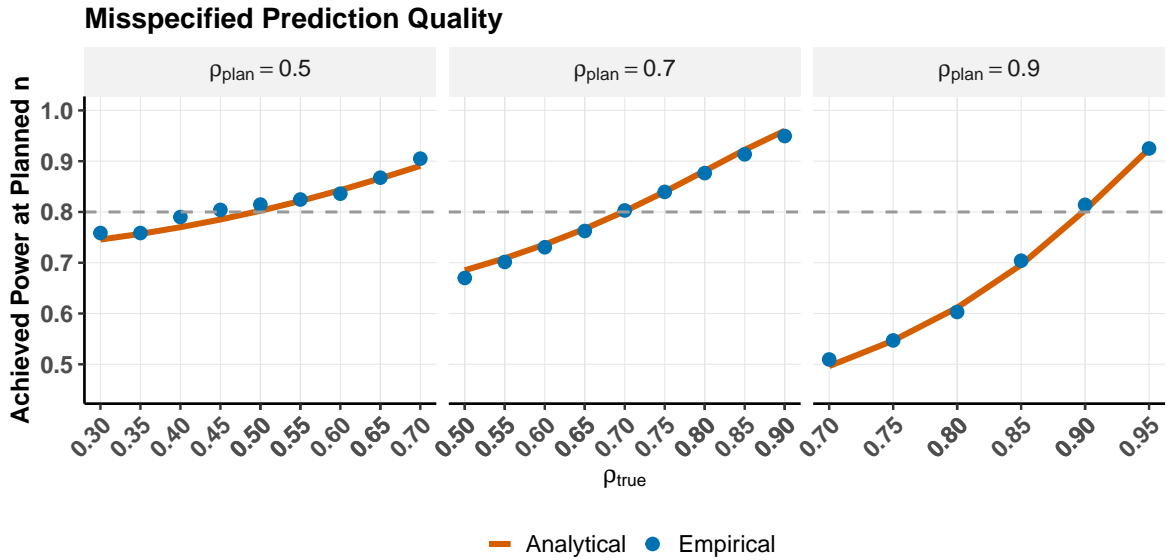


Figure S14: Sensitivity to misspecified prediction quality. The dashed line marks the target power, while each panel varies the true prediction quality around the value used at the planning stage.

**Distributional robustness.** Log-normal (right-skewed) and  $t_5$  (heavy-tailed) outcomes probe how far the Gaussian approximation can be pushed. For  $t_5$  outcomes, agreement remains tight, whereas the log-normal setting shows larger discrepancies in the most skewed, small- $n$  regime; see Figure S15.

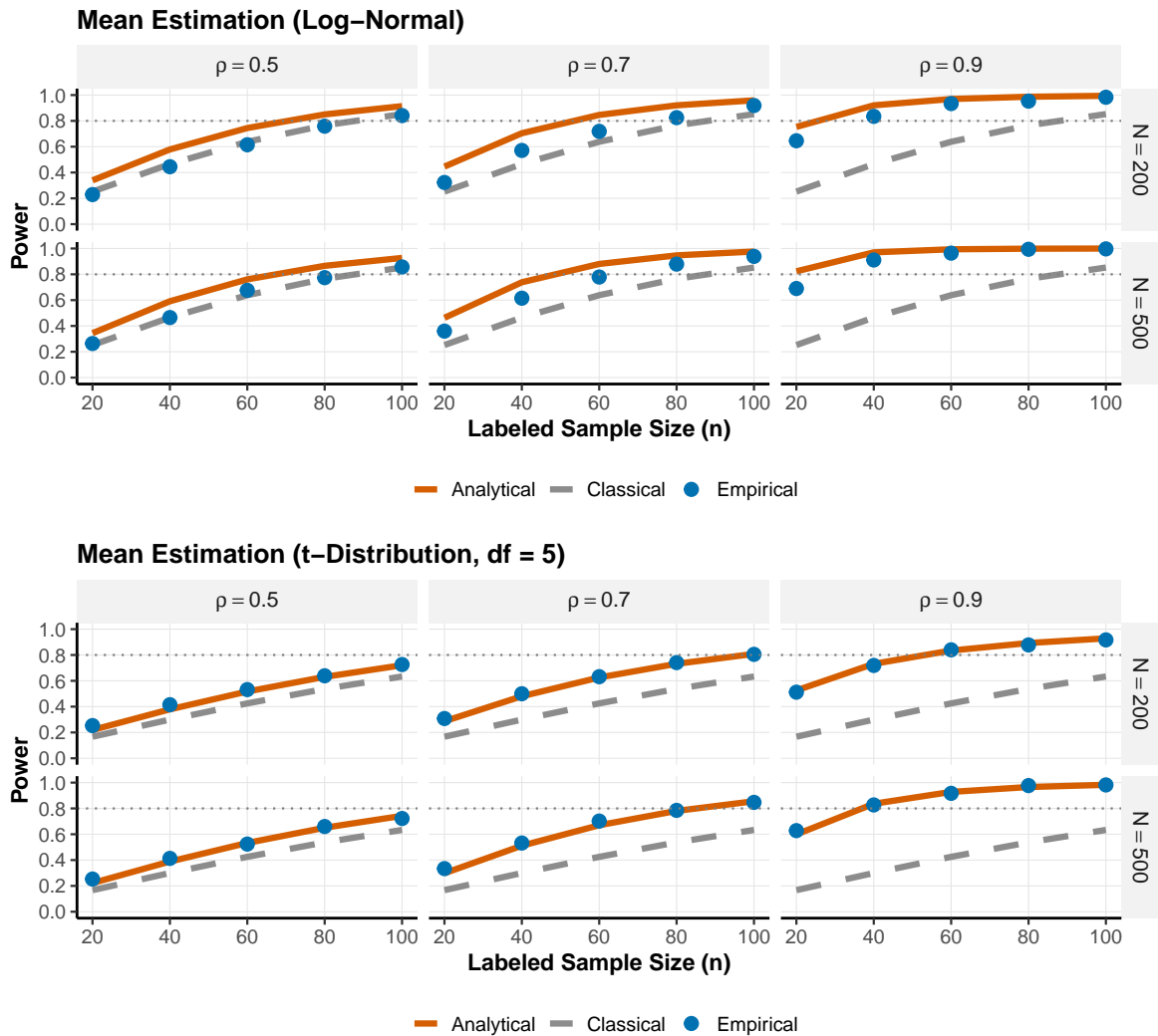


Figure S15: Distributional robustness for the one-sample mean problem. Top: log-normal outcomes, where the CLT-based formula overshoots at small  $n$  under severe skew (max discrepancy 0.144 at  $n = 50$ ,  $\rho = 0.5$ ). Bottom:  $t_5$  outcomes, where agreement remains tight despite heavy tails (max discrepancy 0.018).